Rec'd, Nasa Repr. RQT-3448

NASA CR-54102

McDonnell Report A984

Analysis Of An Arc-jet Exhaust

by

W.M. Van Camp
F.D. McVey
D.W. Esker
R.J. Checkley
S.E. Morrifield
C.K. Murch
J.H. Painter
V.S. Scognamiglio

prepared for

National Aeronautics And Space Administration

Contract NAS 3-3562

MCDONNELL

RESEARCH DIVISION

December 1964

Requests for copies of this report should be referred to:

National Aeronautics and Space Administration
Office of Scientific and Technical Information
Washington, D.C. 20546
Attention: AFSS-A

NASA CR-54102
McDonnell Report A984

Final Report

Analysis Of An Arc-jet Exhaust

by
W.M. Van Camp
F.D. McVey
D.W. Esker
R.J. Checkley
S.E. Merrifield
C.K. Murch
J.H. Painter
V.S. Scognamiglio

prepared for
National Aeronautics And Space Administration
December 1964
Contract NAS 3-3562

Technical Managers
NASA - Lewis Research Center
Electric Propulsion Office
Joseph Czika
Henry R. Hunczak

RESEARCH DIVISION
MCDONNELL AIRCRAFT CORPORATION
LAMBERT - ST. LOUIS MUNICIPAL AIRPORT, BOX 516, ST. LOUIS 66, MO.

Preface

The work described in this report was performed by McDonnell Aircraft Corporation under Contract NAS3–3562 for the Lewis Research Center of the National Aeronautics and Space Administration. The contract period was July 11, 1963 through July 10, 1964. Messrs. Henry Hunczak and Joseph Czika of NASA were technical managers of the program.

The work was accomplished in the Plasma Physics Research Laboratories under the direction of W.M. Van Camp. The project leader was F. D. McVey.

The persons responsible for the research projects included in this program were:

Arc-jet thrustors	*C. K. Murch* *J. H. Painter*
Thrust	*C. K. Murch*
Enthalpy and mass flux	*D. W. Esker*
Velocity	*S. E. Merrifield*
Electron beam	*R. J. Checkley*
Langmuir probe	*V. S. Scognamiglio*

Other professional personnel who contributed to the program were R. H. Clark, W. G. Duke, A. J. Theiler, and R.A. Williamson.

Contents

Summary

The purpose of the work reported herein was the development of techniques for measuring the performance characteristics and nozzle exit plane plasma parameters of hydrogen arc-jet thrustors operating in the power range of 17 to 33 kw and vacuum exhaust conditions of 0.40 to 1.40 torr.

The plasma parameters to be measured in the nozzle exit plane were stagnation enthalpy, mass flux, gas velocity, gas density, and electron density. The arc-jet performance measurements included thrust and specific impulse. The experimental diagnostic equipment used were a thrust balance, a stagnation enthalpy and mass flux probe, a photometric velocity meter, an electron beam, and a Langmuir probe.

The arc-jet used in the development of the diagnostic techniques was a vortex stabilized, water-cooled unit using hydrogen as the propellant. It had a throat diameter of 0.254 inches, a nozzle exit plane diameter of 1.46 inches, and was operated at two nominal conditions: nozzle exit plane bulk stagnation enthalpies of 45,000 and 60,000 B/lb and corresponding specific impulses of 840 and 970 seconds.

Two radiation-cooled hydrogen arc-jet thrustors having constrictor diameters of 0.15 and 0.25 inches were operated in the vacuum system in preparation for nozzle exit plane and performance measurements. The arc powers ranged from 7.7 to 36.6 kw and the flow rates varied from 3.59×10^{-4} to 6.00×10^{-4} lb/sec.

The thrust and specific impulse characteristics of the arc-jet were obtained with the thrust stand over the range of power levels from 17 to 33 kw and hydrogen flow rates of 2.9 to 5.4×10^{-4} lb/sec. The measured thrust varied from 0.26 to 0.40 lb and the specific impulse ranged from 770 to 1000 sec.

Stagnation enthalpy profiles at the exit plane of the arc-jet operating at bulk stagnation enthalpy levels of 39,000, 45,000 and 60,000 B/lb were obtained with the stagnation enthalpy probe. The profiles peaked at the jet centerline with a maximum value of 87,000 B/lb measured at the 60,000 B/lb operating condition.

Qualitative mass flux profiles were obtained at the nozzle exit plane. However, integration of these profiles accounted for only 50% of the metered propellant flow rate. It is possible that the probe lip did not properly swallow the normal shock.

The nozzle exit plane velocity profile measurements at the nominal 45,000 B/lb jet enthalpy condition showed a peak velocity of 42,000 ft/sec decreasing to 22,000 ft/sec 0.5 inches off the axis. The results also showed a sensitivity to the frequency of the signals being observed.

Electron beam attenuation measurements made in varying density environments of hydrogen, helium, and argon were not reproducible. Comparison of the present transmission ratios with the calculated requirements for density profiles in the exhaust of a hydrogen arc-jet indicates that the present equipment is inadequate.

Langmuir probe measurements at the nozzle exit plane gave electron densities of 2.6×10^{11} *to* 5.8×10^{11} *electrons/cm*^{3}.

It is anticipated that perfection of these experimental and analytical techniques and their application in analyzing arc-jet performance characteristics will result in a better understanding of the processes occurring in arc-jets and will lead to designs having improved performance characteristics.

1 Introduction

Considerable effort has been spent in recent years to develop arc-jet thrustors for space propulsion missions such as attitude control, station keeping, change of orbit, and earth-moon ferry. However, it is significant to note that this work has progressed without a comprehensive knowledge and understanding of the fundamental processes occuring in the device. For example, information is lacking concerning the mechanism of energy transfer to the electrodes; the flow conditions at the nozzle throat due to non-uniformities of the arc process; the freezing of species as a result of rapid expansion of the jet; the relative contributions of thermal expansion and magnetohydrodynamic forces in the production of thrust; and the mechanism by which electrical energy is transferred to the propellant.

It is evident that a knowledge and understanding of these phenomena are necessary before arc-jet devices having improved performance characteristics can be developed. It is also apparent that the primary restriction to the knowledge of such processes is the lack of reliable experimental techniques for measuring the plasma properties in arc-jet thrustors along with their corresponding performance characteristics.

The objective of the work reported herein was the investigation of techniques for measuring nozzle exit plane plasma parameters and performance characteristics of arc-jet thrustors using hydrogen as the propellant. The plasma parameters to be measured in the nozzle exit plane included total enthalpy, mass flux, gas velocity, gas density, and electron concentration. The measurement techniques to be investigated included a thrust stand a stagnation enthalpy and mass flux probe, a photometric velocity meter, an electron beam density device, and a Langmuir probe.

The research work described in this report is a follow-on to Contract NAS8–2519. The work on the initial contract (Ref. 1.1) resulted in the concentration of effort in this program on the development of the most promising diagnostic techniques for the measurement of the nozzle exit plane flow conditions and performance characteristics of 30 kw hydrogen arc-jet thrustors. Once the diagnostic techniques are successfully developed, they will be used to establish a model of the flow and energy exchange processes occurring in the arc-jet.

Reference

1.1 W. M. Van Camp, F. D. McVey, S. E. Merrifield, J. H. Painter, R. W. Vogel, R. H. Clark, F. J. Brock, and R. L. Fox, "Hydrogen Arc-jet Exhaust Diagnostics," McDonnell Report 9621 (August 1963) Final Report on Contract NAS8–2519.

2 Arc-jet thrustors

2.1 Water-cooled arc-jet

The development of the arc-jet diagnostic techniques described in this report required a stable, repeatable, and readily attainable hydrogen exhaust jet having local properties similar to those of the high temperature, radiation-cooled thrustors. A water-cooled, vortex stabilized hydrogen arc-jet* was designed, built and operated for this purpose. The range of operating and performance parameters for this engine are given in Table 2.2, page 7.

The arc-jet developed for this diagnostic program is shown in Fig. 2.1. The cathode of the arc was a 0.625 inch diameter rod positioned by a water-cooled holder. The anode was a convergent-divergent water-cooled nozzle having a convergence angle of 35^{o}, a divergence angle of 15^{o}, a throat diameter of 0.254 inches and an exit plane diameter of 1.46 inches (area ratio of 32.9). The nozzle anode was electrically insulated from the cathode by a dielectric sleeve that formed a part of the cylindrical arc chamber. The propellant was injected tangentially into the arc chamber through four 0.025 inch diameter ports inserted through the insulated sleeve. The ports were sized to yield sonic injection for a maximum radial pressure gradient in the arc chamber and hence a stable arc on the centerline of the nozzle. The engine design was flexible in that the cathode position, the arc chamber volume, the injection port diameters, the nozzle configuration and the cathode shape could be easily varied. An arc chamber pressure tap was located on the rear chamber wall.

The nozzle expansion ratio was the maximum possible consistent with proper expansion and the pumping characteristics of the vacuum system used. The arc-jet was instrumented for determination of power level, arc-efficiency, and system pressures.

Figure 2.2 shows the hydrogen arc-jet firing into the vacuum tank.

2.2 Arc-jet test facilities

The subsystems necessary for the operation of the hydrogen arc-jet were an electrical power supply, a vacuum system, instrumentation, a propellant supply, and a cooling water supply.

Power supplies

The initial development tests (Ref. 1.1) and the first 23 diagnostic tests of the present program (Table 9.1, pages 55 and 56) were performed with an ignitron tube power supply. This power supply consisted of two parallel rectifiers using Class D ignitrons in half-wave bridges. The output voltage

* *The arc-jet thrustors, thrust stand, and specialized diagnostic devices in these studies were designed and constructed under McDonnell's independent research programs.*

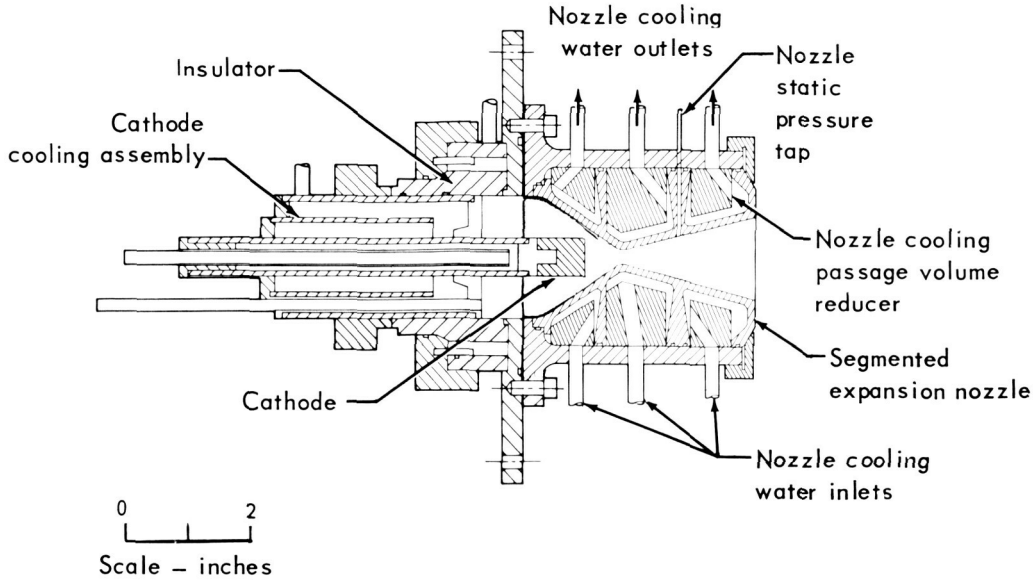

Fig. 2.1 Water-cooled 30 kw arc-jet

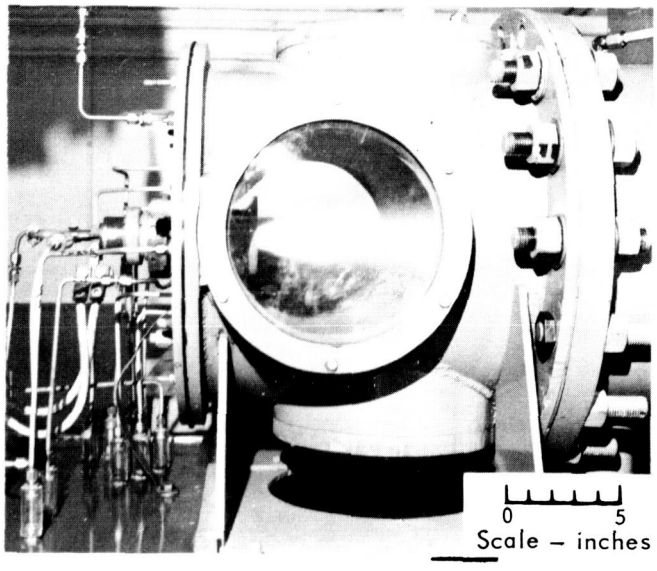

Fig. 2.2 Water-cooled 30 kw hydrogen arc-jet exhausting into vacuum tank

was virtually constant at 400 volts. The necessary droop in the output voltage characteristic was provided by water-cooled stainless steel tubes used as series resistors in the circuit. These tubes provided seven resistance steps of 0.13 ohms each and one additional step of 0.75 ohms.

All tests in the present program subsequent to the first 23 (Table 9.1 through 9.4, pages 55 through 59 were conducted with a dry rectifier 60 kw power supply. This power supply has a three phase full-wave rectifier with saturable reactor current control providing the necessary drooping output characteristic. To obtain the necessary minimum sparking potential of hydrogen, a 400 volt open circuit voltage was used.

Future electric propulsion research requiring higher power will utilize McDonnell's two 1 Mw, three phase, full-wave rectifiers power supplies with saturable reactor control.

Vacuum system

The vacuum pumping system consisted of two mechanical booster assemblies, a holding pump, four sixteen inch diameter oil booster pumps, and other valving, filters, and piping. The system has a pumping capacity of 4×10^{-4} lb/sec of hydrogen plasma at 0.80 torr. A two-stage heat exchanger consisting of water and liquid nitrogen baffles was located in the vacuum tank to protect the pumping system and improve the pumping characteristics.

Arc-jet installation

Figure 2.3 is a schematic diagram of the hydrogen arc-jet installation. The arc-jet was mounted with all instrumentation external to the vacuum system and the mounting plate was electrically isolated from the grounded tank. This allowed a minimum of vacuum pass-throughs and the placement of a current metering shunt between the plate and ground.

The arc-jet mounting plate was attached to the end of an eighteen inch diameter cylindrical test section with four 10 inch diameter observation ports. The arc-jet cooling water was supplied at a constant head from a 55 gallon reservoir by a turbine water pump.

Hydrogen was supplied to the engine from eight 2000 psi storage bottles manifolded and regulated to 200 psi supply pressure. The flow was then throttled by a needle valve into a critical nozzle flowmeter. The stagnation pressure upstream of the flowmeter was used in conjunction with precision calibrations to set the flow rate.

A three junction copper-constantan differential thermopile was used to measure the cooling water temperature rise for determining the efficiency of the arc-jet.

Instrumentation

The instrumentation of the hydrogen arc-jet and vacuum system was designed to measure the parameters shown in Table 2.1. All electrical signals were continuously recorded in a direct print oscillograph at a paper speed of 0.25 inches per second.

Table 2.1 Description of instrumentation

Parameter	Measurement	Method of measurement
Power input	Arc voltage	DC voltmeter and oscillograph recording of voltage divider network
	Arc current	DC ammeter and oscillograph recording of 50 mv shunt output
Propellant flow rate	Flowmeter pressure	Bourdon gauge and oscillograph recording of transducer output
	Flowmeter temperature	Oscillograph recording of copper-constantan thermocouple
Power loss	Cooling water temperature differential	Oscillograph recording of copper-constantan differential thermocouple
	Cooling water flow rate	"Rotameter" flow meter
System pressures	Arc chamber	Aneroid gauge and oscillograph recording of transducer output
	Ambient exhaust (vacuum)	Thermopile gauge, ionization gauge, and oscillograph recording of ionization gauge output

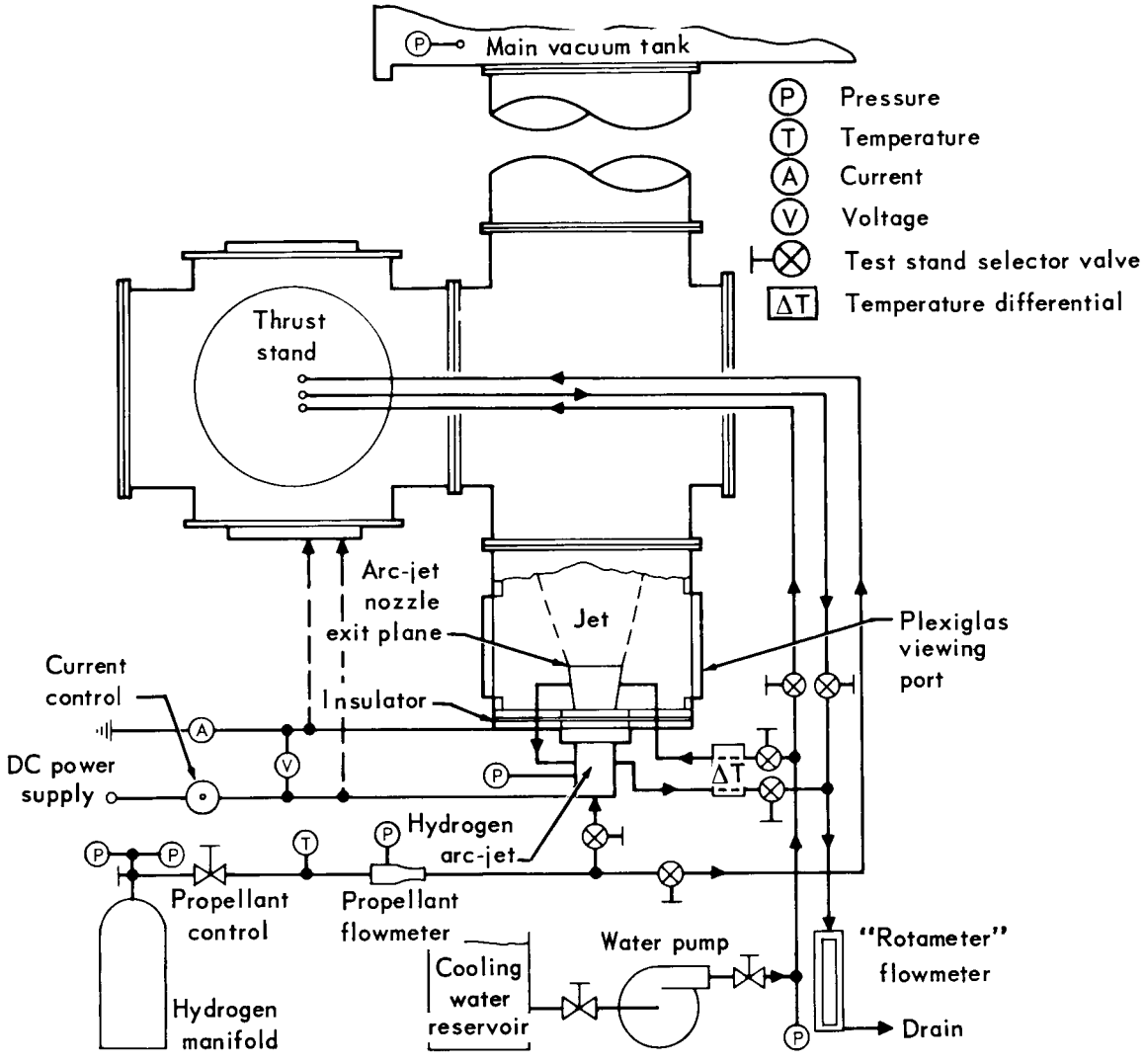

Fig. 2.3 Test installation for water-cooled arc-jet

2.3 Test procedure

Prior to starting the hydrogen arc-jet, the test section and arc chamber were evacuated and purged with an inert gas. Hydrogen was then introduced into the arc chamber until the pressure exceeded 50 torr at which time an open circuit voltage of 400 volts was applied across the electrodes of the arc-jet. The hydrogen flow was then stopped. When the arc chamber pressure fell to approximately 2 torr the arc initiated at which time the hydrogen flow was initiated stabilizing the arc. The desired operating condition was then set by adjusting either the hydrogen flow and/or the supply current.

Visual observations were made during operation to insure proper expansion of the gas in the nozzle. It was required that the ratio of the ambient exhaust pressure to the arc chamber pressure be less than 0.007 (Ref. 1.1) and that the bright region of the first normal shock in the stream was at least three diameters downstream of the exit plane.

During the test a continuous oscillograph recording was made of all operating parameters except the cooling water flow rate. When a test was made using a diagnostic device, the water flow rate and many of the same operating parameters being recorded on the oscillograph were read and recorded (Table 2.1).

Normal shut down consisted of turning off the power supply, then the hydrogen flow, followed by an inert gas purge of the vacuum system.

When mounted on the thrust stand the arc-jet was started in a different manner. The hydrogen flow rate was preset; then a solenoid valve in the propellant feed line was closed and the arc chamber evacuated to 0.002 torr; an open circuit voltage of 400 volts was applied across the electrodes and the solenoid valve was opened; when the pressure-gap product in the arc chamber reached the lower sparking point, the arc ignited and the arc-jet stabilized at the preset hydrogen flow rate.

2.4 Operating conditions for diagnostic tests

The scope of the diagnostic technique development program entailed demonstration of the technical feasibility of the diagnostic devices at two different specific impulse levels. The operating characteristics of the water-cooled arc-jet had previously been determined (Ref. 1.1), but no performance measurements had been made. To determine the performance characteristics, tests were made using the thrust stand described in Section 3. The operating parameter ranges for these tests are given in Table 2.2 and Fig. 2.4.

Table 2.2 Water-cooled hydrogen arc-jet operating and performance parameter ranges

Parameter	Maximum	Minimum
Hydrogen flow rate (lb/sec)	5.40×10^{-4}	2.91×10^{-4}
Nozzle exit plane bulk average stagnation enthalpy (B/lb)	64,400	28,400
Arc chamber pressure (torr)	279	180
Ambient exhaust pressure (torr)	1.40	0.38
Power input (kw)	33	17
Thermal efficiency (%)	81.4	58.0
Specific impulse (sec)	1050	650
Thrust (lb)	0.40	0.26

These performance measurements along with the requirements of proper propellant expansion, stability, and repeatability were used to establish the engine operating conditions given in Table 2.3 as the two primary diagnostic test conditions.

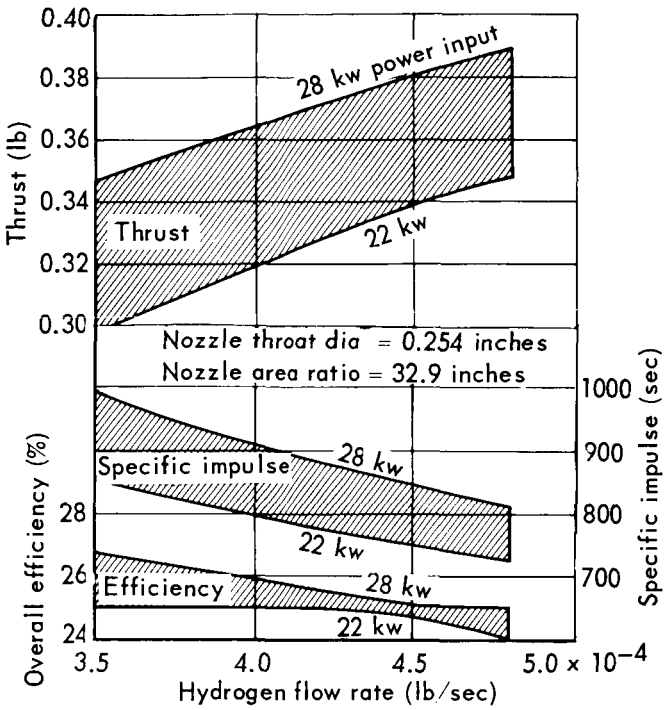

Fig. 2.4 Performance ranges for water-cooled hydrogen arc-jet

Table 2.3 Primary operating conditions for diagnostic tests

Arc chamber pressure (torr)	Power input (kw)	Propellant flow rate (lb/sec)	Nozzle exit plane bulk average stagnation enthalpy(B/lb)	Specific impulse (sec)
187	22.4	3.6×10^{-4}	45,000	840
205	28.0	3.6×10^{-4}	60,000	970

A third operating point, 39,000 B/lb bulk average jet stagnation enthalpy, was also used in the development of the enthalpy probe tip. Numerous intermediate jet enthalpy levels were used in the preliminary tests with the velocity meter as well as the thrust stand. A complete tabulation of the arc-jet operating conditions for the various diagnostic experiments is presented in Tables 9.1 through 9.4 in the Appendices.

2.5 *Radiation-cooled arc-jets*

The radiation-cooled arc-jet to be used for the performance tests and for the nozzle exit plane diagnostic measurements is shown in Fig. 2.5. In preparation for these tests, two thrustors of this type were mounted on the cooled thrust stand (Figs. 3.2 and 3.7) and checked out in the vacuum system. The two thrustors differed only in the diameter and length of the constrictor as shown in Fig. 2.5.

In running these preliminary tests, it was desired to establish a satisfactory starting procedure; to determine the vacuum system performance using the high temperature engines; to establish the time required for the engine to stabilize and reach thermal equilibrium when changing from one operating condition to another; and to determine the magnitude of the zero shift problem that occurred during the thrust measurements on the water-cooled arc-jet.

Table 2.4 shows the range of performance parameters for the check out tests of the two radiation-cooled arc-jets using hydrogen as the propellant. Four tests were performed on thrustor A; two in which the mass flow was held constant. The two tests on thrustor B were performed with variable mass flows. Both arc-jets operated stably with no apparent sputtering.

The first step of the starting procedure for operating the radiation-cooled arc-jets was to preset the hydrogen flow rate at 5.5×10^{-4} lb/sec.

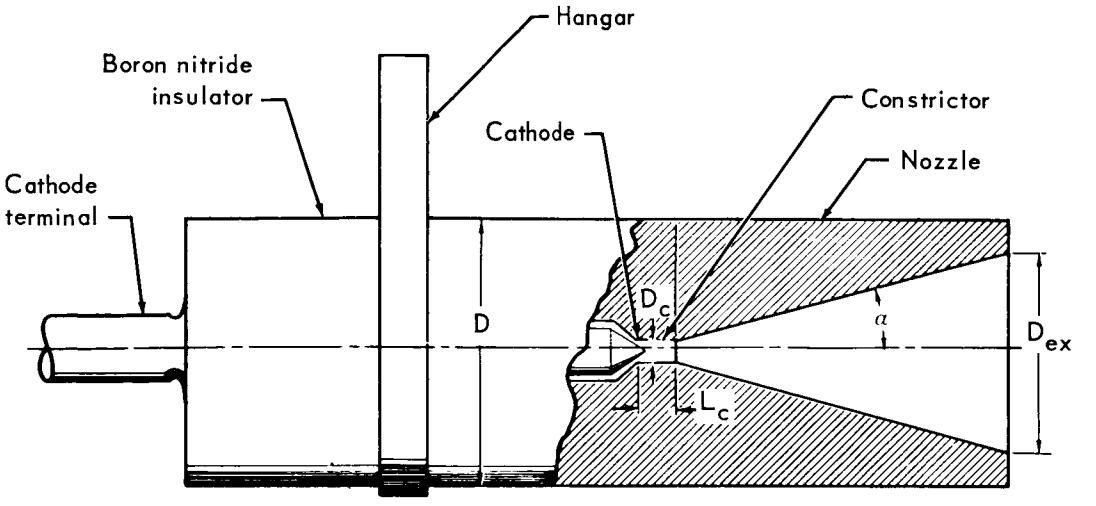

Note: All dimensions are in inches

	D	D_c	D_{ex}	L_c	α
Thrustor A	1.875	0.150	1.500	0.300	15°
Thrustor B	2.000	0.250	1.500	0.500	15°

Fig. 2.5 Radiation-cooled 30 kw arc-jet

Table 2.4 Operating ranges for radiation-cooled hydrogen arc-jet check out tests

	Thrustor A		Thrustor B	
	Maximum	Minimum	Maximum	Minimum
Hydrogen flow rate (lb/sec)	6.00×10^{-4}	4.09×10^{-4}	5.52×10^{-4}	2.59×10^{-4}
Arc voltage (volts)	198	69	150	110
Arc current (amps)	207	39	255	54
Arc power (kw)	35.3	7.7	36.6	8.1
Arc chamber pressure (torr)	1022	619	522	280
Vacuum tank pressure (torr)	3.02	0.87	2.84	1.71

A quick acting solenoid valve, between the flowmeter and the thrustor, was then closed and the arc chamber was evacuated to 0.05 torr. With the saturable control reactor on the power supply adjusted for minimum power output, an open circuit voltage of 400 volts was applied to the electrodes. To initiate the arc the propellant solenoid valve was then opened and the arc-jet stabilized at the preset flow rate and a power input of approximately 7.7 kw. Increases in the power

input were made by adjusting the saturable control reactor to achieve a higher arc current. In order to avoid damage to the tungsten nozzle, the power was increased at a nominal rate of 2.5 kw every 7 minutes until the 15 kw level was reached. The power was then increased at a rate of 5 kw every 7 minutes to the desired operating power level.

The first test on thrustor A resulted in an overheating of the vacuum tank and portions of the heat exchanger inside the tank. Subsequent tests proved that a water jacket solved the tank heating problem and baffles alleviated the heat exchanger problem. Table 2.4 shows the pressure in the vacuum tank ranged from 0.87 to 3.02 torr.

The stabilization period required for thermal equilibrium was determined by maintaining the engine operating conditions constant for a period of 15 minutes and then increasing the power by 5 kw. The thrust increased immediately as the power was increased and continued to increase more slowly for approximately 5 minutes. At this point the arc-jet was judged to have achieved thermal equilibrium.

The zero shift of the thrust transducer during these tests prevented the accurate measurement of thrust. The support rods for the thrust stand are being replaced by Kovar to minimize the effect of thermal expansion. Also, tests will be made to determine the temperature sensitivity of the transducer element.

Figure 2.6 shows that the radiation calorimeter is a double walled, water-cooled copper cylinder which completely encloses the arc-jet except at the nozzle exit. The device is designed to minimize the conductive heat paths between the arc-jet and the cooled inner wall. Measurements of coolant flow rate and coolant temperature differential are used to calculate the power lost through radiation from the arc-jet thrustor.

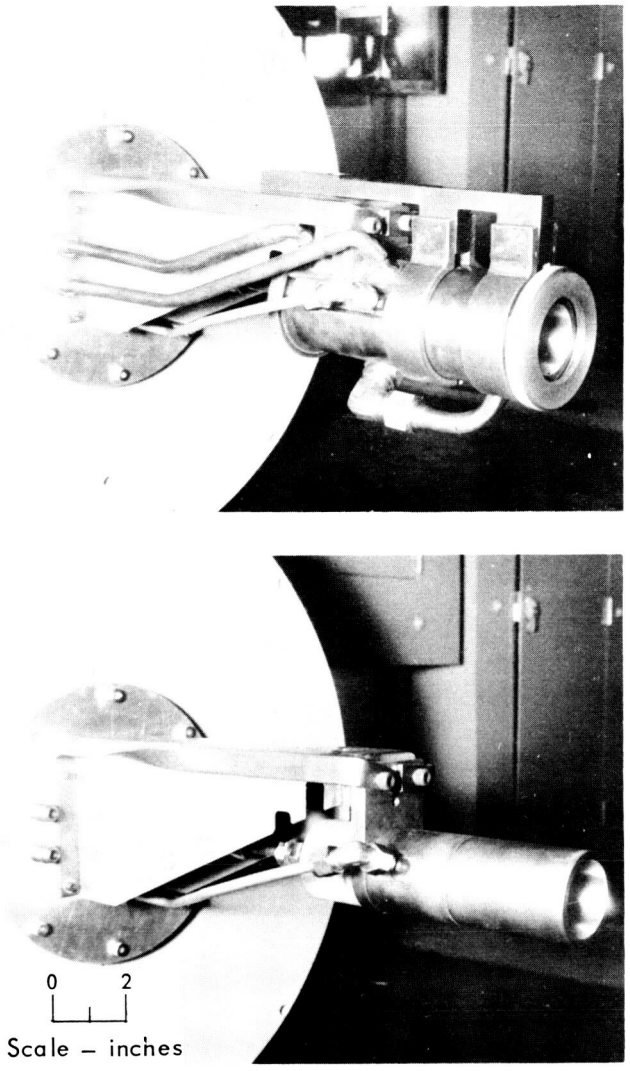

Fig. 2.6 Radiation-cooled 30 kw arc-jet with and without radiation calorimeter

3 Thrust

This work was aimed at developing a technique for measuring the thrust of water and radiation-cooled 30 kw arc-jets exhausting into a vacuum tank.

3.1 *Thrust stand for water-cooled arc-jet*

In designing the thrust stand, consideration was given to the following requirements:

- Thrust measurements were to be made in the range of 0.1 to 1.0 pounds.
- The hydrogen arc-jets required flexible instrumentation leads, coolant lines, and power connections that could produce nonlinearity, friction, and mechanical hysteresis if the system deflected appreciably.
- The vacuum system in which the thrust measuring device was installed was subject to mechanical vibrations and, therefore, detrimental vibrational modes had to be attenuated by the support structure.
- The system was to operate under vacuum conditions and was subject to non-uniform heating of its components.
- A high level of electrical noise from the arc-jet required shielding of electrical components.

The thrust stand designed for the laboratory type water-cooled arc-jets is shown in Figs. 3.1 and 3.2. The specification that led to the general configuration of the system was that of mechanical isolation from the vacuum tank. The flexure system was designed to reduce vibrations in all but the vertical plane. The force transducer was relatively insensitive to all forces except those in the direction of thrust.

The hydrogen arc-jet was mounted on the lower platform which was displaced by the thrust developed by the arc-jet. The force transducer on the lower platform was connected to the upper platform by means of a thin cable. The thrust produced very small relative deflections between the platforms but deflected the entire double pendulum system. The tension in the connecting cable, as measured by the force transducer, was equal to the thrust of the arc-jet minus any tare loads which included the forces due to stiffness of the coolant and propellant lines and the flexures. To minimize the tare loading, the deflection was kept small by adding approximately 200 pounds weight to the system.

The lower flexure system of the thrust stand consisted of 0.035 inch diameter braided steel cable. Coolant was supplied to the arc-jet by Tygon tubing. The propellant line consisted of 20 feet of 1/4 inch diameter copper tubing wound in a helix 3 feet long and 3 inches in diameter. The inherent stiffness of power cables capable of carry-

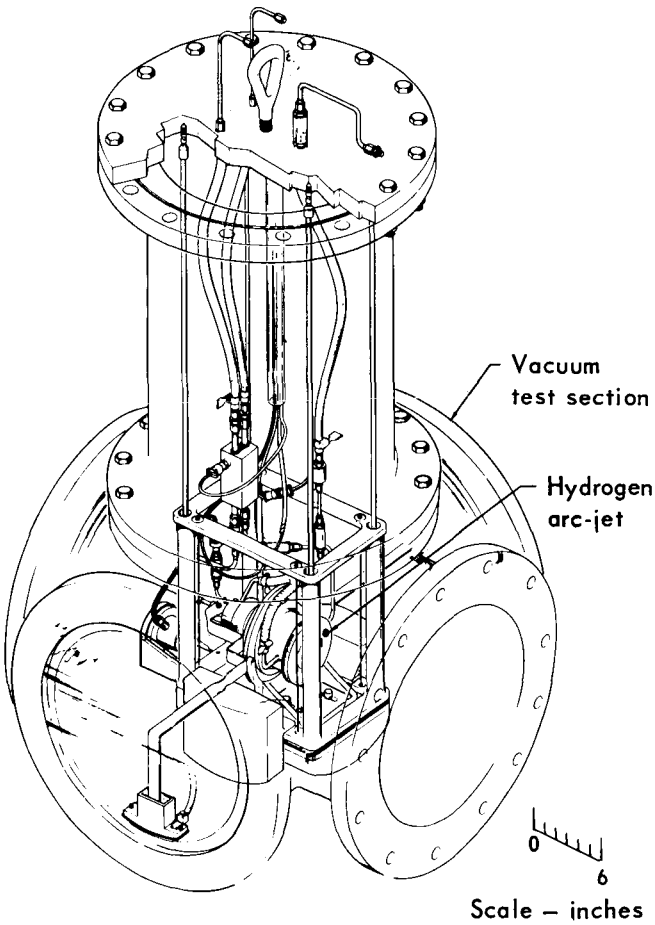

Fig. 3.1 Arc-jet thrust stand

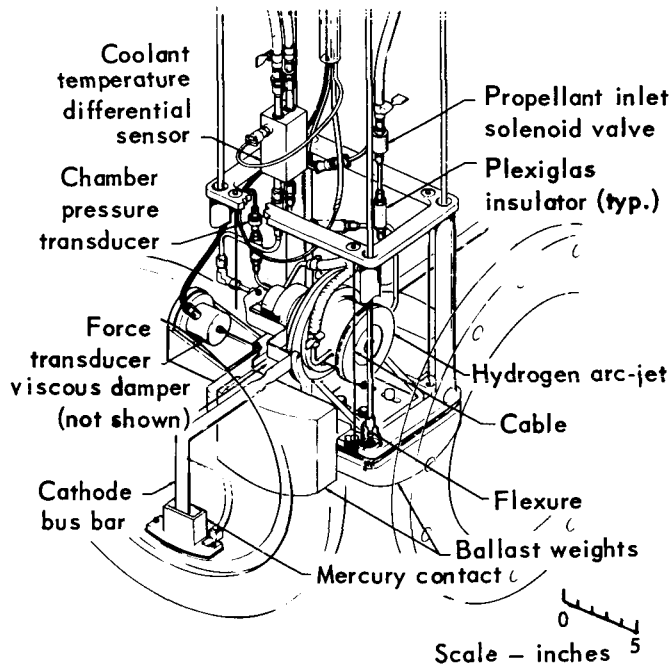

Fig. 3.2 Detail view of arc-jet thrust stand

ing 200 amperes made necessary the use of copper bus bars which terminated in pools of mercury. Total tare loading of the system with all instrumentation installed and with coolant and propellant lines pressurized was less than 10% of the thrust to be measured. Calibration of the system indicated that friction and mechanical hysteresis were not present. The small tare loading (inherent in any system if allowed to deflect) did not produce a nonlinearity in the calibration and was repeatable.

The system was calibrated by means of standard weights. A fine wire connected to the lower platform passed through a hole in the vacuum chamber and over a precision pulley. Weights hung on the wire simulated a known thrust and an accurate calibration was obtained. Since an absolute calibration of the load cell was known, the tare of the system was obtained by comparison of the calibration curves. The system was calibrated before and after each test. The calibration method also allowed the addition of standard weights while the arc-jet was operating as a check on the slope of the calibration curve.

The possibility of arcing external to the engine was eliminated by electrically isolating the vacuum chamber test section and thrust stand structure from ground and by carefully insulating all components that were above ground potential. The mercury surfaces were covered with silicone fluid to prevent arcing.

3.2 *Thrust measurements for water-cooled arc-jet*

A total of 43 tests were performed on the water-cooled arc-jet configuration described in Section 2. The purpose of these tests was to demonstrate the reliability of the thrust measuring system over the operating range of the arc-jet. Table 2.2, page 7 shows the range of operating and performance characteristics for these tests.

For one series of tests a single representative propellant flow rate was chosen and reproduced as accurately as possible from test to test. The power input to the arc-jet was then varied from a lower limit defined by arc-jet instability to an upper limit defined by the power supply. Figure 3.3 illustrates the dependence of thrust and specific impulse on the power input at a fixed propellant flow rate. The percent deviation of measured propellant flow rate throughout these tests was 2.9%. The thrust data are reproducible to within ±1.5%.

For another series of tests a high initial flow rate was chosen and the output of the power supply set at a predetermined value. The flow rate was then decreased. The variation in propellant flow rate caused a variation in the power input. Each individual operating condition was accurately reproduced from test to test.

Figure 3.4 shows the thrust and propellant flow rate data at three power levels. For these tests the electrode gap (nozzle throat to cathode surface) was 0.75 inches, the nozzle area ratio was 32.9, the throat diameter was 0.254 inches, and the propellant was injected tangentially through four 0.025 inch diameter orifices on a 1.063 inch radius. In Fig. 3.4, the data are reproducible to within ±1.5%, ±2.5%, and ±7%, depending on the power level. These results indicate that the reproducibility of the measurement of thrust is

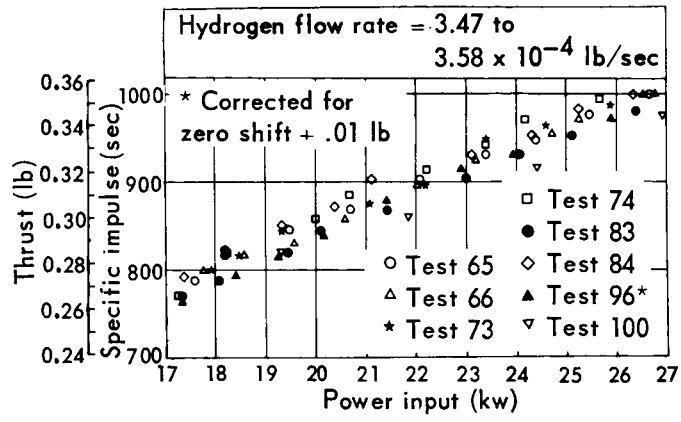

Fig. 3.3 Hydrogen arc-jet thrust and specific impulse characteristics

a function of power input.

Figure 3.5 shows data taken from a series of tests over a large portion of the region of stable operation of the arc-jet.

The dependence of the thrust measurements on the temperature of the thrust stand structure is illustrated in Fig. 3.6. The thrust and the temperature of the structure near the nozzle exit are plotted versus time. The temperature of the structure caused by heating near the nozzle exit plane is apparently a function of the jet enthalpy and the duration of the test. This figure shows a typical high power test with both the power input and propellant flow rate constant (32.5 kw and 3.90 x 10^{-4} lb/sec). The temperature of the structure continually increased until the power to the arc-jet was turned off. The structural temperature then decreased. The measured thrust increased with increasing time and temperature for constant operating conditions. The cold flow thrust level measured after the power was turned off is also shown. When the propellant flow was terminated, a zero shift in the measured thrust existed. Its magnitude was approximately the same

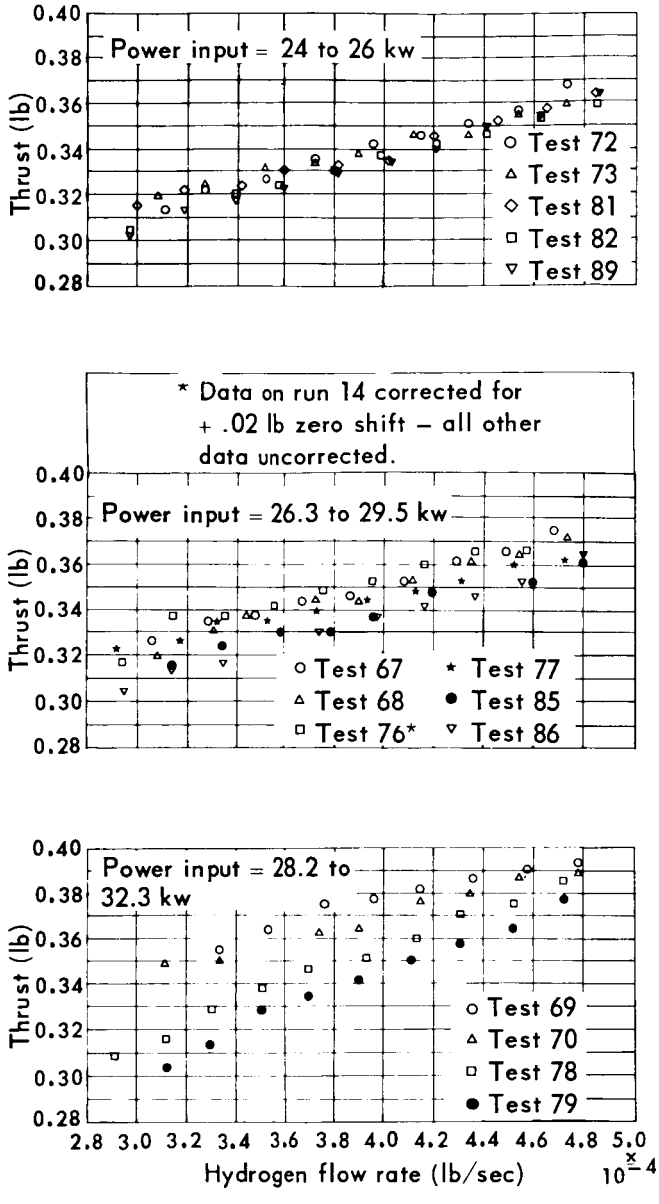

Fig. 3.4 Hydrogen arc-jet thrust characteristics

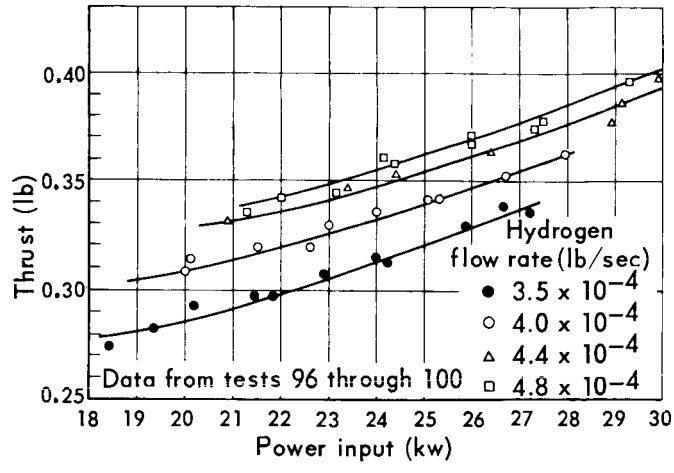

Fig. 3.5 Hydrogen arc-jet thrust characteristics

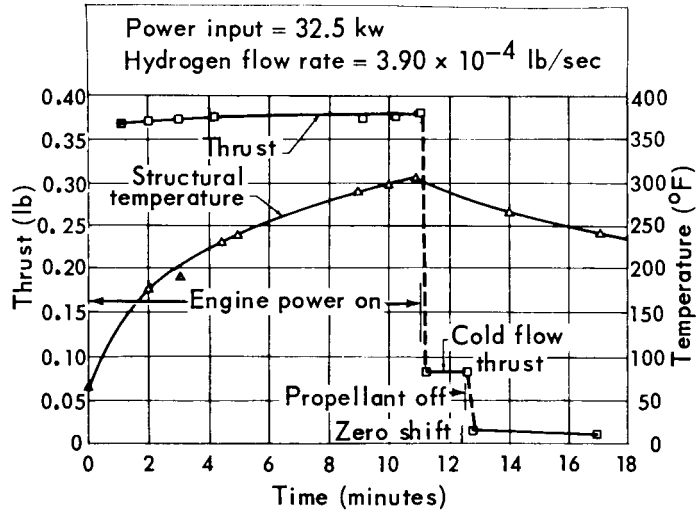

Fig. 3.6 Thrust data showing zero shift

as the time dependent increase in thrust. The thrust signal eventually returned to zero as the system cooled. The discontinuities in the figure represent changes in thrust level which were accompanied by oscillations of the thrust stand at the natural frequency of the suspension system.

It appears that the zero shift accounts for most of the spread of the thrust data and that it is time dependent. Since the test time varied from less than two minutes to about 25 minutes, the zero shift error was not repetitive and could be controlled by limiting the test duration.

3.3 *Thrust stand for radiation-cooled arc-jets*

Modifications were made to the thrust stand so that thrust measurements could be made using the high temperature radiation-cooled 30 kw arc-jet configuration. This unit is shown in Figs. 3.7 and 3.8. The higher operating temperatures of the radiation-cooled arc-jet dictated the design of a cooled thrust stand. It used a double pendulum suspension system similar to the previous configuration. The radiation-cooled arc-jet was mounted underneath the lower platform which tended to be displaced by the thrust developed by the arc-jet. The force transducer, also mounted on the lower platform, was connected to the upper platform by a thin cable and a zero adjustment mechanism. The force transducer allowed only a very small relative deflection between the platforms; therefore, the entire system deflected. The tension in the connecting cable, as measured by the force transducer, was equal to the thrust of the arc-jet minus tare forces due to stiffness of the cable flexures and the propellant line.

The container attached to the lower platform (which enclosed the suspension system and force transducer) was filled with a damping fluid maintained at near constant temperature by a heat exchanger attached to the upper platform.

A polished stainless steel shield was mounted between the arc-jet and the bottom of the thrust stand to intercept much of the heat that would otherwise be absorbed by the oil container. Further thermal isolation of the arc-jet was accomplished by ceramic insulators in the propellant line and chamber pressure tap and a boron nitride wafer in the arc-jet mount.

The arc-jet was electrically isolated from the thrust stand. Power to the thrustor was supplied by stainelss steel and copper bus bars which terminated in pools of mercury. Fiberglass tape was used to electrically insulate those protions of the arc-jet and bus bars that were above ground potential.

Instrumentation of the system provided measurements of thrust, arc chamber pressure, voltage, current, propellant flow rate, vacuum chamber pressure, and structural temperatures at several points on the arc-jet and thrust stand. All of the parameters were continuously recorded during a test by a direct readout oscillograph.

An attachment point for a calibration wire was provided on the chamber pressure transducer line at the centerline of the thrustor. The calibration procedure was similar to that previously described for the uncooled thrust stand.

Six tests were performed using this cooled thrust stand and two high temperature, radiation-cooled arc-jets as described in Section 2.5. The primary purpose of these preliminary tests was to checkout the arc-jets, the associated instrumentation and thrust stand, and to establish operating procedures for subsequent tests.

These tests indicated that there was a significant zero shift problem. Since it appears that the shift is temperature dependent, the support rods are being replaced by Kovar material and improved thermal isolation of the force transducer is in work.

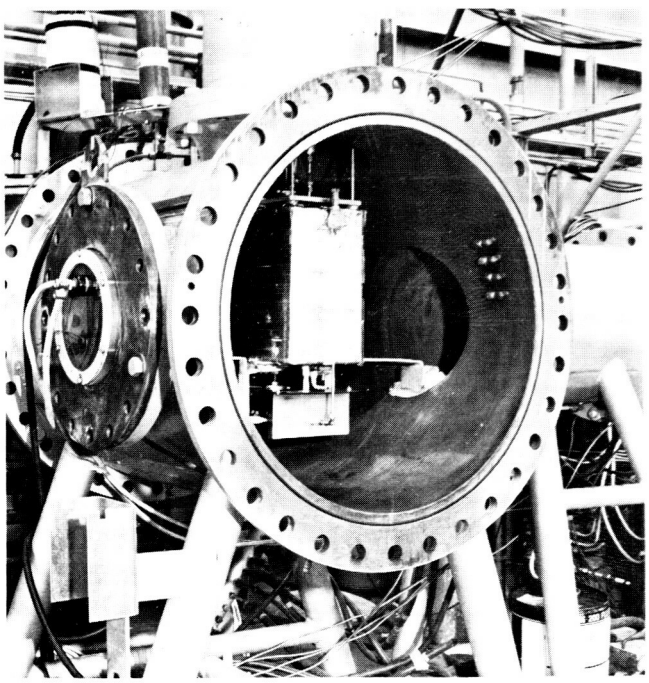

Fig. 3.7 Radiation-cooled arc-jet mounted on thrust stand in vacuum tank

3.4 Conclusions

The results of the 30 kw water-cooled hydrogen arc-jet thrust work indicate:

1. The double pendulum thrust stand gives reliable thrust measurements.
2. A slight zero shift of the system occurs during the tests.
3. The spread of data increases with increasing power.
4. The spread of data is attributable to the heating of the thrust stand components and/or the force transducer.

Preliminary thrust measurements on the 30 kw radiation-cooled arc-jets indicated a significant zero shift problem. It is concluded that the force transducer was temperature sensitive and should be thermally isolated.

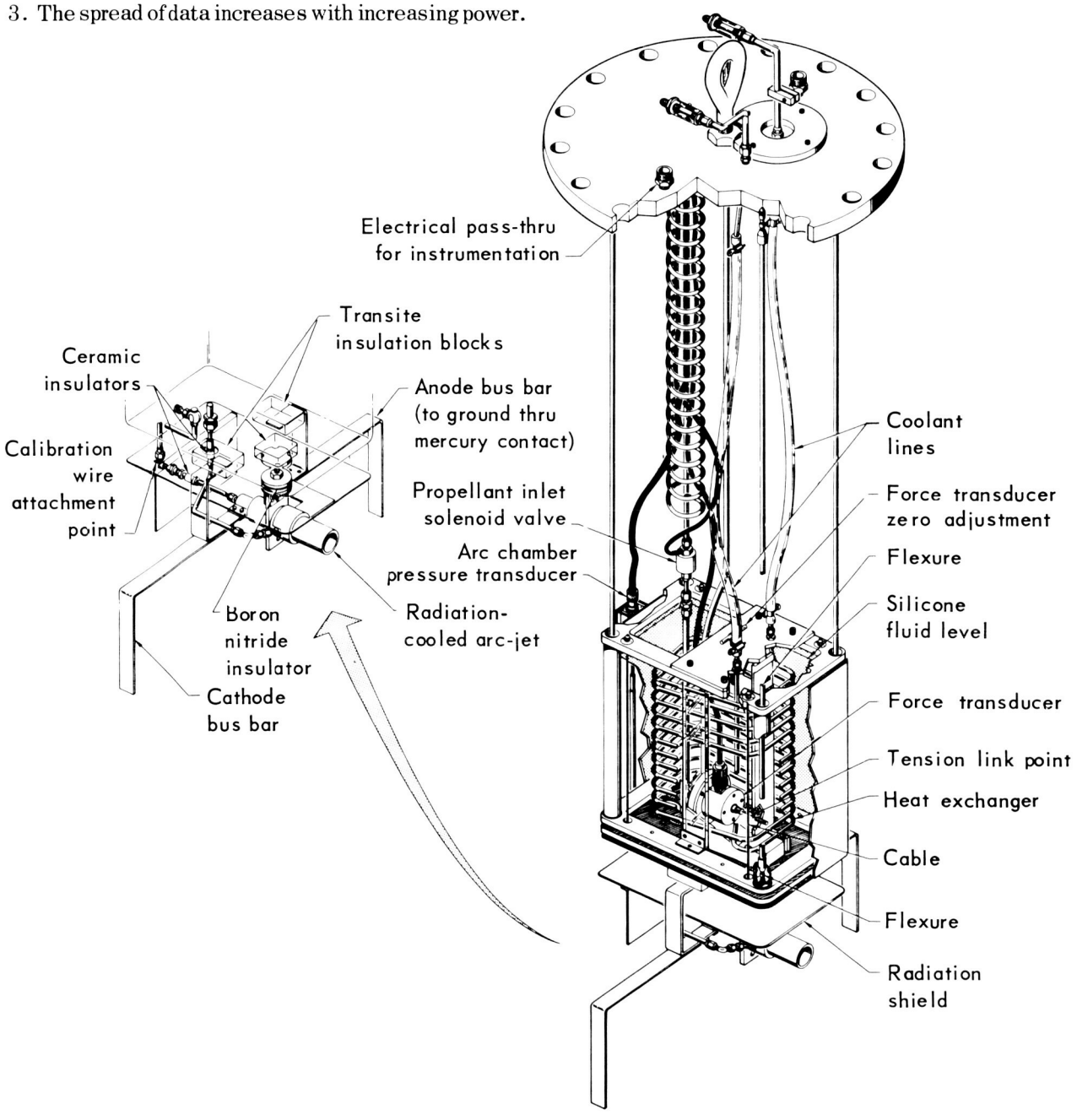

Fig. 3.8 Thrust stand for radiation-cooled thrustors

4 Stagnation enthalpy and mass flux

The purpose of this work was to measure the local stagnation enthalpy and mass flux distribution in the nozzle exit plane of a 30 kw hydrogen arc-jet.

The design chosen to accomplish these measurements was a hollow tube type device having a normal shock inlet. A sample of the supersonic stream is captured by the probe. The energy of the stream sample is then extracted within the probe by cooling water and the mass flow rate through the probe is measured by a sonic flow nozzle at the exit of the probe. If the bow shock is swallowed, the total energy per unit time entering the inner chamber of the probe is the product of the stagnation enthalpy, probe inlet area, local free stream density, and velocity.

The total energy per unit time entering the probe can be accounted for by measuring the temperature rise and flow rate of the cooling water, the total temperature of the exiting gas, and the gas mass flow. The total mass flux across the exit plane and the total stream energy integrated from the probe measurements can be checked against independent measurements of the total mass flow rate and power to the gas in the chamber minus the energy loss in the nozzle.

4.1 Experimental apparatus

Figure 4.1 is a drawing of the stagnation enthalpy probe as initially designed. The probe inlet, the exit sonic flow nozzle, and the heat exchangers are indicated in this figure. The entire probe – except for the inlet lip – was fabricated out of copper. The probe inlet lip diameter of 0.40 inches was a compromise between the heat transfer design con-

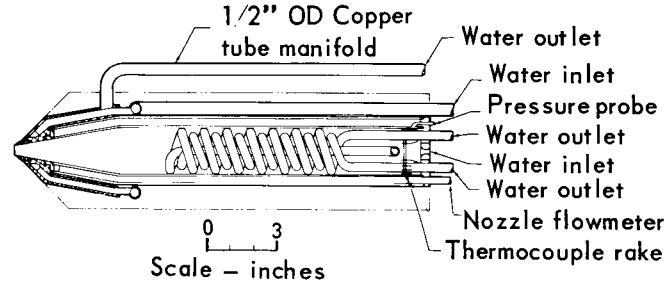

Fig. 4.1 Initial stagnation enthalpy and mass flux probe design

siderations at the lower limit and the anticipated nozzle exit diameter of 4 inches at the upper limit. The probe was designed with two separate cooling systems. System No. 1 is the external cooling jacket in which the probe lip is mounted and which shields the internal cooling system from the jet exhaust. System No. 2 which measures the heat transfer is the internal jacket connected in series with the coiled heat exchanger. Figure 4.1 also shows the pressure tap and the thermocouple rake used to obtain the pressure and temperature of the gas upstream of the exit sonic flow nozzle.

During preliminary checkout tests it was concluded that the initial design of the external cooling jacket did not completely isolate the internal heat transfer of the captured gas sample from the external heat transfer of the surrounding exhaust flow. The external cooling system was replaced by two separate cooling jackets. Figure 4.2 is a drawing of this modified probe design. The cooling systems were fabricated by electroforming the components with copper. The cooling passages were fabricated by machining a solid copper billet to the shape shown in Fig. 4.2. The electroforming was accomplished by techniques which allow the addition of a copper surface over the probe cooling system. An insulating surface was provided between the external and internal cooling system by "potting" No. 8 Sauereisen in the cavity. The probe lip diameter and the overall internal and external probe dimensions were not modified.

Figure 4.3 shows the actuator mechanism that was designed and fabricated to accurately position the enthalpy probe in the arc-jet exhaust. This mechanism consisted of a power driven, water-cooled rod on which the enthalpy probe was mounted. The figure shows this mechanism and the enthalpy probe mounted in the test chamber.

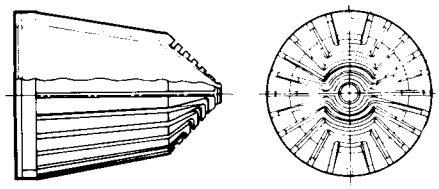

Probe tip omitting outer shell.

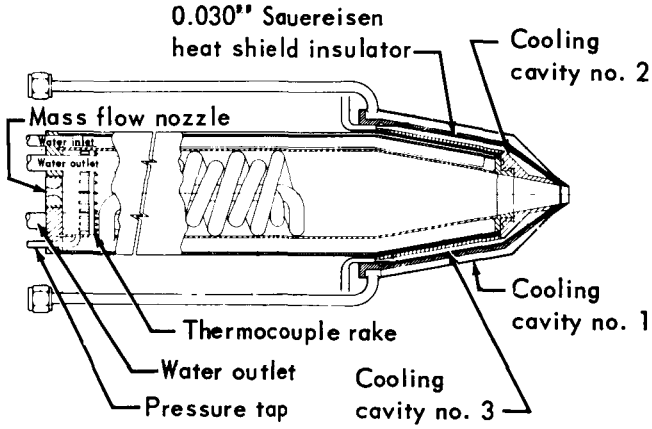

Fig. 4.2 Modified stagnation enthalpy and mass flux probe

4.2 *Mass flow calibration*

Figure 4.4 is a sketch of the system used for calibration of the exit flow nozzles over the range of expected Reynolds numbers. The method of changing the Reynolds number of the calibrating stream was through a change in its temperature. To facilitate this, a gas heater was used to heat nitrogen which was then passed through the cooling system of the probe. This in turn heated the hydrogen passing on through the probe and out the exit nozzle. The hydrogen flow rate was measured with a precision nozzle flowmeter previously calibrated. The calibration was performed in the following steps

(a) The test section was evacuated and hydrogen gas flow was introduced through the precision flowmeter and enthalpy probe.

(b) Nitrogen gas flow was initiated through the shop air heater and enthalpy probe cooling systems after which the heater rheostat was set at a given temperature.

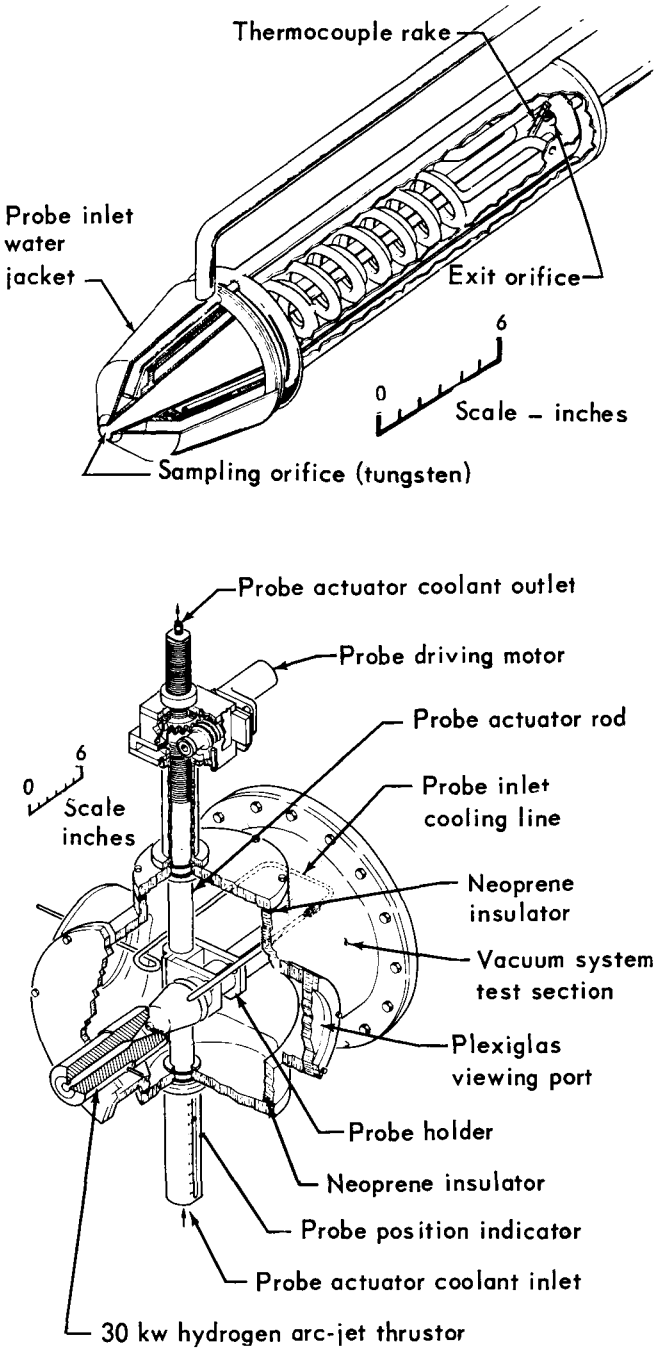

Fig. 4.3 Enthalpy probe installation

(c) The hydrogen flow was then varied through a series of approximately 20 flow rate increments in the range of 2–10 x 10^{-5} lb/sec. At each increment the pressure readings upstream of the precision flowmeter P_{of} and the sonic flow nozzle P_∞ and the gas temperature upstream of the flowmeter T_{of} and the sonic flow nozzle T_∞ were recorded.

(d) The heater rheostat was then set to a higher temperature position and the steps of (c) were repeated. The heater temperature was varied through a range of 100° to 1000°F.

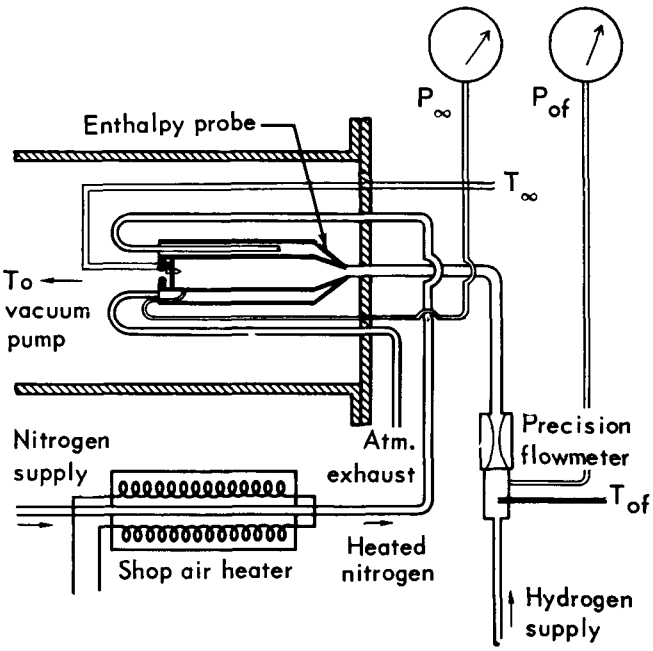

Fig. 4.4 Enthalpy probe calibration system

Figure 4.5 depicts a typical hydrogen mass flow calibration curve for the 0.155 inch diameter sonic flow nozzle. A total of six curves were obtained for each nozzle covering the temperature range of 540°R to 850°R. All the curves are similar in that the data satisfies the following relation at the high flow rates

$$\dot{m} = C_D \frac{P_\infty}{\sqrt{T_\infty}} \quad .$$

The coefficient C_D for each nozzle obtained from the slopes of the calibration curves agrees within 5% of that which would be calculated from

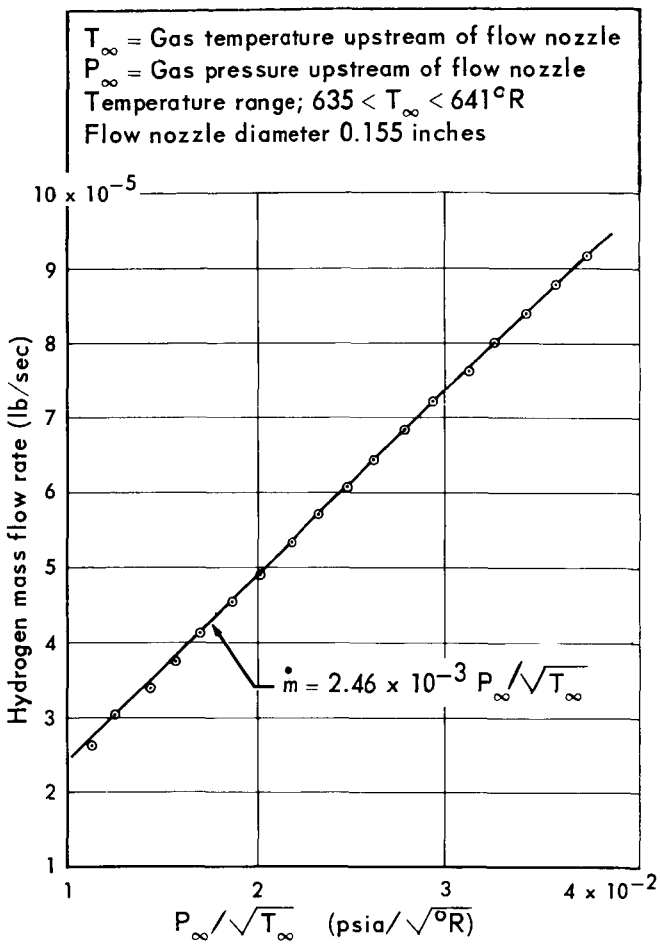

Fig. 4.5 Hydrogen mass flow calibration curve for enthalpy probe flow nozzle

one-dimensional perfect gas relation for a choked nozzle. There appears to be a slight Reynolds number effect in the lower mass flow range as evidenced by the deviation of the data from the straight line plotted.

4.3 *Experimental procedure*

The procedure used to perform the stagnation enthalpy and mass flux experiments was as follows:

(a) The probe was positioned on the centerline of the arc-jet at the nozzle exit plane by means of a centering plug fitted to the nozzle contour and the probe inlet lip. The centerline position was then recorded on the probe actuator.

(b) The probe was then moved to a position approximately 6 inches off the arc-jet centerline and all probe cooling water systems were activated.

(c) The test chamber was then evacuated and the arc-jet started. All instrumentation was then monitored to ascertain when stable operating conditions prevailed.

(d) The probe was then moved into the arc-jet exhaust to a position 0.5 inches off centerline. The water flow rates to the internal cooling systems were adjusted until the inlet and outlet temperature differentials were approximately $15°F$. The position of the normal shock at the probe inlet was observed visually. The pressure and temperature before the exit flow nozzle were then recorded after which the cooling water flow rates were recorded (Table 9.5, page 59).

(e) The probe was then moved across the exit plane in increments of 0.1 inches. At each position the procedure of (d) was repeated. The residence time at each position was approximately five minutes.

(f) After each test termination the probe lip was inspected and the probe lip diameter was measured and recorded.

The tests were performed with the water-cooled hydrogen arc-jet described in Section 2. Table 4.1 shows the arc-jet operating conditions for these tests.

Table 4.1 Nominal test conditions for stagnation enthalpy probe experiments

Arc chamber pressure (torr)	Power input (kw)	Propellant flow rate (lb/sec)	Exit plane stagnation enthalpy (B/lb)	Specific impulse (sec)
222	22.1	4.4×10^{-4}	39,000	770
187	22.4	3.6×10^{-4}	45,000	840
205	28.0	3.6×10^{-4}	60,000	970

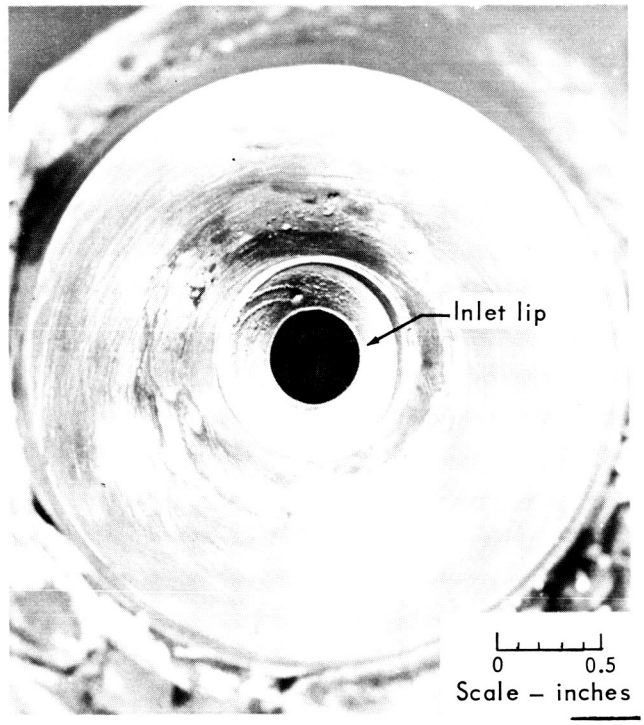

Fig. 4.6 Enthalpy probe showing tungsten lip after 40 minutes of test time

4.4 *Preliminary stagnation enthalpy tests*

Preliminary tests were conducted with the initial design of the enthalpy probe positioned at the nozzle exit plane of the hydrogen arc-jet. These tests indicated that the heat transfer capability of the external and internal cooling systems was sufficient to prevent physical deterioration of the probe and that the internal cooling system effectively cooled the captured gas stream to approximately 500 to 600°R. It was observed that the tungsten inlet lip eroded due to the high heat flux environment. The inlet diameter contracted approximately 5% after the initial run. The contraction rate was reduced upon subsequent runs and after 20 minutes of test time the inlet area contraction remained constant at approximately 9.5% of the original inlet area. Figure 4.6 shows the tungsten lip after approximately 40 minutes of test time.

Figure 4.7 is a drawing of an alternate inlet lip that was designed and fabricated to replace the tungsten lip. This copper lip provided an electroformed water cooling cavity. This inlet lip was used during several tests and the results indicated that the cooled lip could be successfully maintained but imperfections in the electroformed surface were present. Although some leakage occurred on the external surface of the lip, these tests demonstrated the feasibility of using a cooled copper lip for the enthalpy probe.

Figure 4.8 compares the stagnation enthalpy measurements with the probe using both the tungsten lip and the water-cooled copper lip. The distance of the data points from the graph centerline represents the distance between the arc-jet and enthalpy probe axes. These measured nozzle exit plane enthalpy levels were low by a factor of approximately two compared with the value calculated by subtracting the energy lost in the nozzle

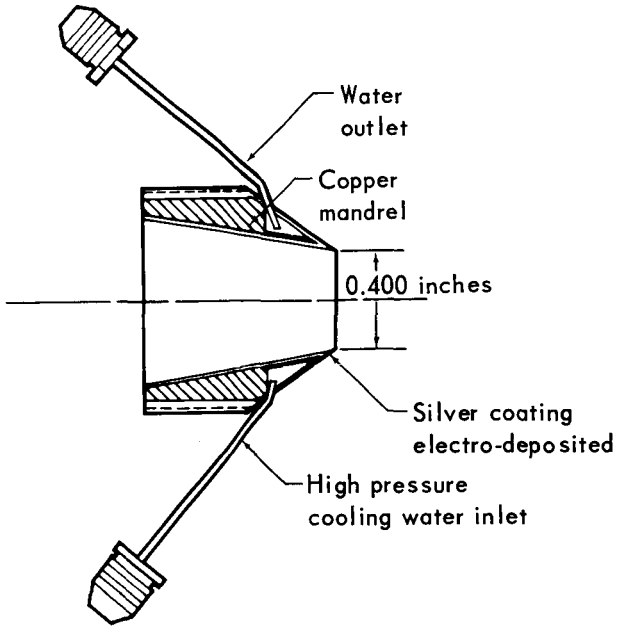

Fig. 4.7 Water-cooled enthalpy probe lip

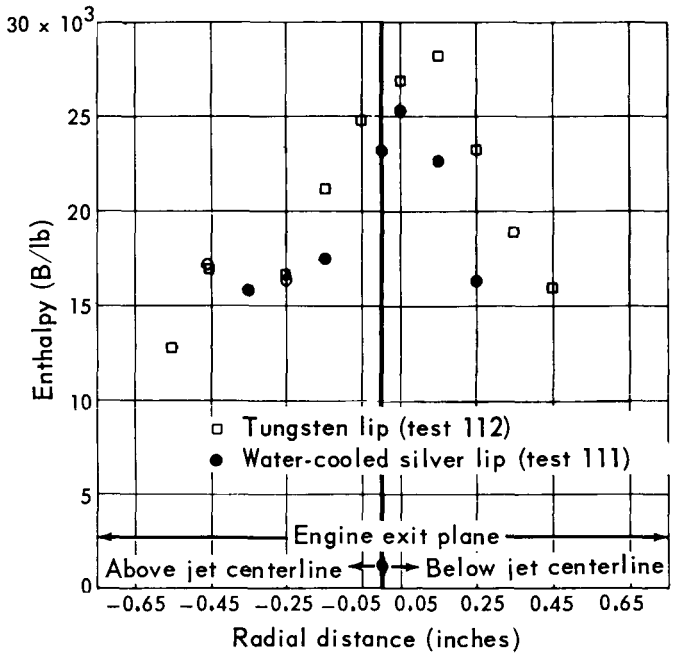

Fig. 4.8 Comparison of stagnation enthalpy probe measurements using tungsten and water-cooled lips

from the energy added in the arc chamber. This suggested that some of the total energy in the captured gas was lost to the probe external cooling system. The external cooling system cools the tungsten lip and extends a distance of approximately three inlet diameters behind the lip leading edge. The energy lost from the captured gas in the neighborhood of the lip was not considered in the energy balance.

As a result of these tests, a redesign of the probe lip and structure holding the lip was initiated. The important features of the redesign were incorporation of a water-cooled copper inlet lip and an external cooling jacket extending 1/4 of an inlet diameter behind the lip leading edge. This modified enthalpy probe is shown in Fig. 4.2. A test of the probe with the redesigned inlet lip and cooling system was performed with the probe positioned on the hydrogen arc-jet nozzle exit plane centerline (Fig. 4.9). The enthalpy level of the exhaust stream was then varied from the low enthalpy design point (I_{sp} = 840 sec) to the high enthalpy design point ($I_{sp} \approx$ 970 sec). During this test a water leak appeared along a discontinuity emanating from the sharp leading edge of the electroformed surface. Visual inspection after the test indicated no physical deterioration of the probe lip nor was the water leak observed during pressure tests with the probe out of the exhaust.

In order to eliminate the leak, the initial electroformed copper plating was machined away and a smooth radius was turned on the leading edge of the lip. A surface of high density copper was then electroformed on this radius and the sharp probe lip was redefined by machining this coating of copper.

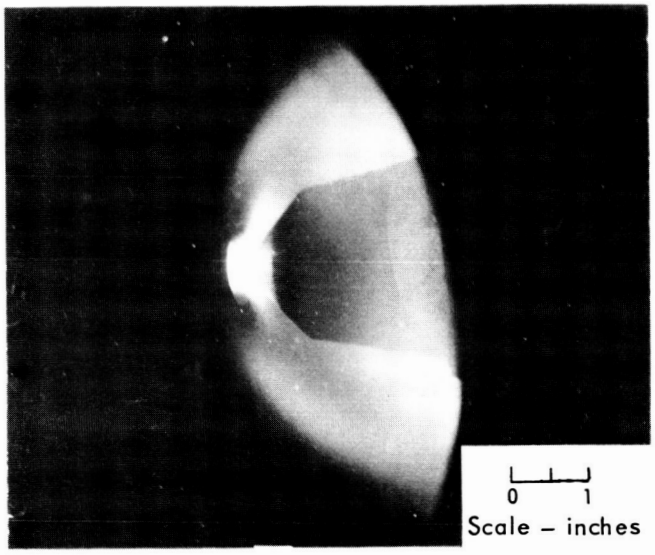

Fig. 4.9 Stagnation enthalpy probe in hydrogen arc-jet exhaust

4.5 *Stagnation enthalpy profile measurements*

Two series of stagnation enthalpy profile measurements were performed at ten positions along a diameter of the nozzle exit plane. The first series of tests were conducted at exit plane bulk stagnation enthalpy levels of 39,000, 45,000, and 60,000 B/lb; the second series at 39,000 and 45,000 B/lb. The results of these tests and the corresponding arc-jet operating conditions are shown in Fig. 4.10. The probe performed satisfactorily during the first series of tests at the two lower enthalpy levels. Visual observations indicated that the normal shock appeared to be standing off the probe lip and that the jet was deflected onto the thermocouples at the rear of the probe when the probe was positioned below the centerline. The vacuum chamber pressure for those tests was 2.50 torr. As the probe was passed through the exhaust centerline at the bulk stagnation enthalpy level of 60,000 B/lb (centerline stagnation enthalpy approximately 87,000 B/lb) a leak developed at the probe lip leading edge. Sealing this water leak involved machining away the plated copper to a point only a few thousandths of an inch from the water cavity. The entire lip surface was joined with high temperature silver solder and the water cavity was leak checked with 600 psig water pressure thd found to be devoid of leaks. High density copper was then plated over this silver soldered surface to redefine the sharp probe lip. In addition, a shield was placed over the thermocouples at the rear of the probe to reduce the heat transfer from the deflected jet when the probe was positioned below the jet centerline.

The second series of tests were then performed at enthalpy levels of 39,000 and 45,000 B/lb. Visual observation of the flow during these tests indicated that the normal shock at the probe lip appeared to be swallowed. The vacuum chamber pressure was 1.75 torr. The stagnation enthalpy profile results in Fig. 4.10 indicate that the 39,000 and 45,000 B/lb profiles in the first series of tests were reproduced in the second series. Also the level of enthalpy values are close to the bulk average values calculated from an energy balance. This shows that the cooling passage design changes incorporated in the present probe represent a significant improvement compared to the previous design.

The data scatter observable at radial positions beyond 0.4 inches indicates that further effort will be required to determine the enthalpy profile in this region.

The enthalpy measurements below the jet centerline were of questionable accuracy due to the jet deflecting into the region of the thermocouples used to measure the cooling water temperature. Also, since the values below the jet centerline were lower for the second series of tests, it appears that the shield placed over the thermocouples reduced the jet impingement effect.

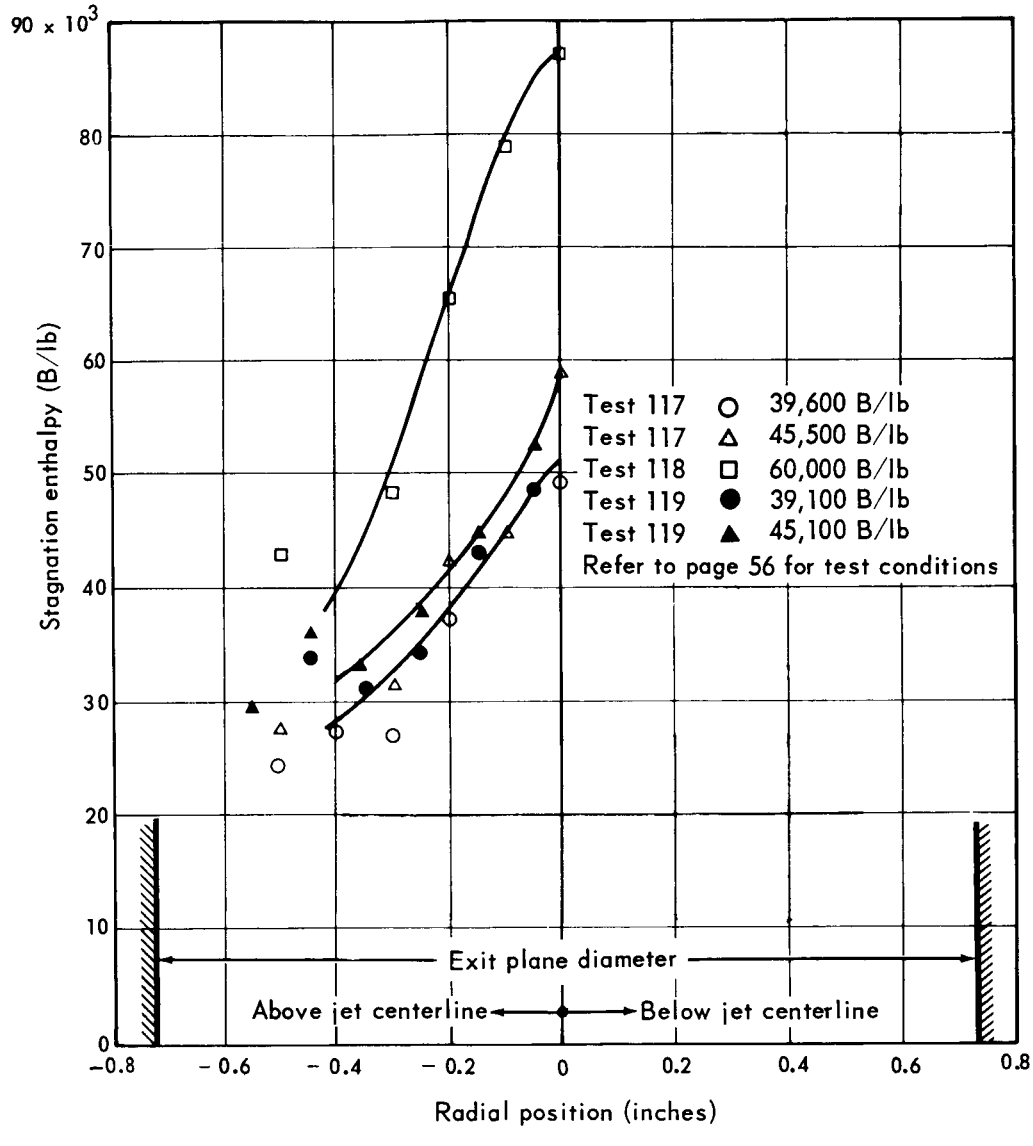

Fig. 4.10 Arc-jet exhaust stagnation enthalpy profiles

4.6 Preliminary mass flux experiments

The gas mass flux measurements obtained during the second series of stagnation enthalpy profile tests (Section 4.5) are shown in Fig. 4.11. The mass flux was determined by dividing the measured mass flow rate through the probe by the inlet area at the probe lip (0.124 in^2). The integration of the mass flux distribution across the nozzle exit plane should equal the total mass flow through the arc-jet thrustor. That is:

$$\dot{m} = \int_0^{r_o} 2\pi \rho \, v \, r \, dr,$$

where $\dot{m}$ = mass flow,
r = variable radius,
r_o = nozzle exit plane radius,
v = velocity,
ρ = density.

The integration of the above equation was obtained graphically by plotting ρv versus r^2. The integral thus becomes

$$\dot{m} = \pi \int_0^{r_o^2} \rho v \, d(r^2)$$

and the total mass flow equals the area under the curve multiplied by π.

Table 4.2 shows the comparison of the integrated mass flux profiles with the mass flow measured in the propellant inlet line to the arc-jet by a critical nozzle flowmeter.

The data in Table 4.2 indicates that the measured propellant mass flow was approximately double the integrated mass flux values. Complete checks on instrumentation and calculation procedures were made in an attempt to explain this discrepancy. Since no significant errors were found, it was concluded that the normal shock at the probe lip was not properly swallowed and the distributions of Fig. 4.11 are not quantitatively accurate.

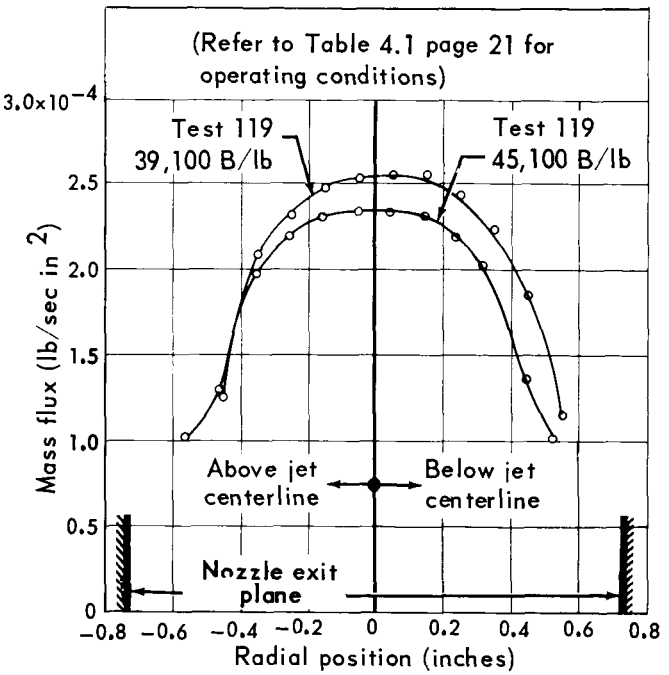

Fig. 4.11 Mass flux profiles in hydrogen arc-jet exhaust

Table 4.2 Mass flow comparisons

Test no.	Integrated mass flow rate (lb/sec)	Metered mass flow rate (lb/sec)
119	2.29×10^{-4}	4.41×10^{-4}
119	1.89×10^{-4}	3.54×10^{-4}

4.7 Conclusions

1. The test results showed that local stagnation enthalpies can be measured in the exhaust of a 30 kw hydrogen arc-jet using a water-cooled probe without physical deterioration or damage under local stagnation enthalpy levels up to approximately 87,000 B/lb. (This was the centerline enthalpy for the 60,000 B/lb bulk average stagnation enthalpy tests.)

2. The measured stagnation enthalpy values reproduce and compare favorable with the values predicted from an energy balance.

3. The discrepancy between the measured propellant mass flow and the integrated mass flux indicates that the present probe design is inadequate for local mass flux measurements. It is possible that the discrepancy is due to the local flow field conditions at the probe inlet.

4. Separate stagnation enthalpy and mass flux probes are desirable. This is due to the incompatibility of the sharp leading edge requirements of the mass flux probe and the large leading edges necessitated by the cooling requirements of the enthalpy probe.

5 Photometric velocity

The objective of the velocity study was to investigate the feasibility of determining hydrogen arc-jet exhaust velocity profiles by photometrically sensing the random light intensity fluctuations inherent in the luminous plasma stream. These fluctuations are sensed at two fixed stations in the exhaust and the time required to traverse the known distances between the two stations is measured and used to calculate the velocity. This technique is entirely passive in that the stream is in no way physically disturbed by the measurement. It should also be noted that the method assumes the light fluctuations are traveling at the stream velocity. This method was suggested by the observation of high frequency light fluctuations in smear photographs of the exhaust of a 30 kw hydrogen arc-jet. (Ref. 1.1).

5.1 Experimental apparatus

The initial velocity meter design incorporated type 1P28 photomultiplier tubes and two entrance apertures which were separated by 1.7 inches. To record the data, Polaroid photographs were taken of the single sweep of a dual beam oscilloscope. Each beam of the oscilloscope displayed the output signal of a photomultiplier.

Apparent plasma stream velocities were established with this device, but due to the limited sensitivity of the photomultipliers, the minimum plasma sampling diameter was approximately 0.3 inches. Typical centerline velocities near the nozzle exit for a fully expanded 30 kw hydrogen arc-jet (0.254 inch throat diameter, 32.9 exit area ratio) were in the region of 40,000 to 50,000 ft/sec. Velocities off the centerline were somewhat lower. As a result of the limited sensitivity of this system, data could be recorded only for those operating conditions which gave an exhaust region of intense luminosity. Also, the large sampling areas prohibited accurate velocity profile measurements. These limitations prompted the design and fabrication of the velocity meter described in the following paragraphs.

A sketch of the second velocity meter design is shown in Fig. 5.1 and a diagram of the experimental test arrangement is shown in Fig. 5.2. The photomultiplier tubes have a response range of 3000 to 7500 angstroms with maximum radiant sensitivity of 0.6 amp/μwatt at 4200 angstroms. The outputs of the photomultiplier tubes are channeled through 400 cycle high pass filters into a dual beam oscilloscope. A Polaroid camera was mounted on the oscilloscope for photographing the single sweep traces.

As shown in Fig. 5.2, each optical path for light received by the photomultipliers contains three apertures and a lens. Aperture 1 determines the size of the plasma sample; aperture 2 reduces stray radiation incident through aperture 1; and aperture 3 provides the light source for the lens

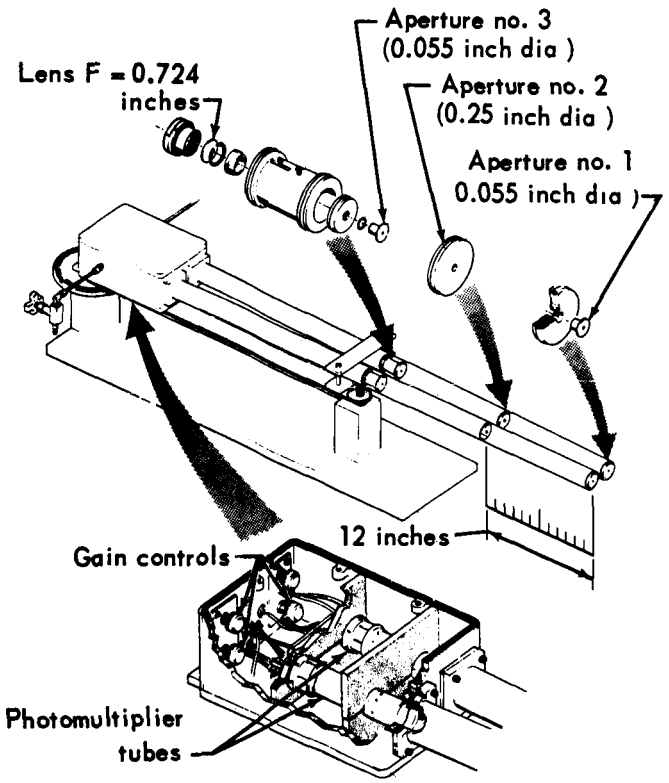

Fig. 5.1 Velocity meter and components

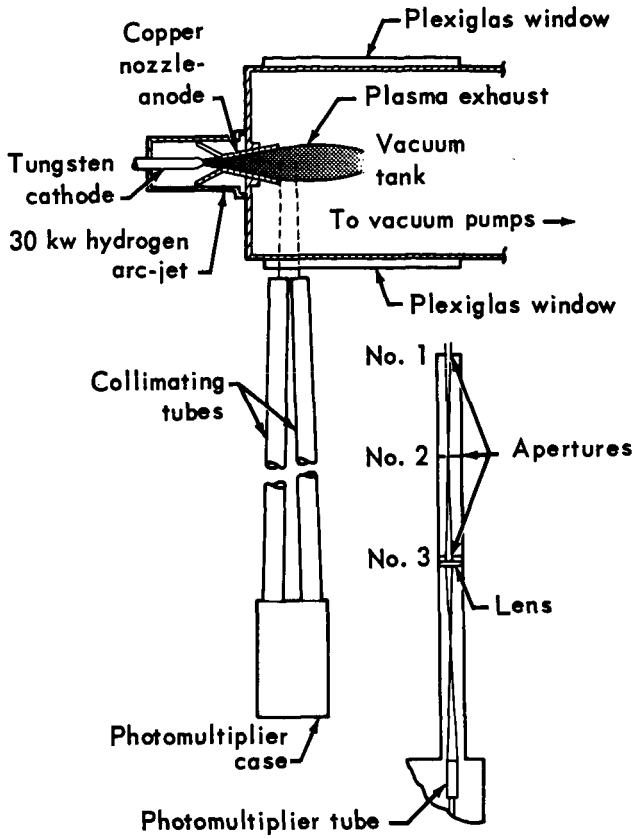

Fig. 5.2 Velocity meter test arrangement

which distributes the light over the photosensitive cathode of the photomultiplier tube. The aperture discs and lenses are contained in the 48 inch long, 2 inch diameter, stainless steel, light collimating tubes.

The velocity meter is moveable in the vertical plane and possesses an accurate adjustment for obtaining exhaust profile data.

5.2 *Investigation of signal characteristics*

By performing experiments with the second velocity meter design, the nature of the photomultiplier signals was examined to determine the frequencies which could be readily used for the calculation of jet velocity. The light source for these experiments was the axial centerline at the nozzle exit of a 30 kw water-cooled, hydrogen arc-jet. These observations of the signal characteristics indicated;

- that a constant amplitude (dc) component of high magnitude was present
- that a 180 cps variation (360 cps when the arc power supply was full wave rectified) was superimposed on the constant ampli-

tude component with a peak-to-peak magnitude being approximately 1/3 of the constant amplitude component. The source of this variation was attributed to the fundamental frequency of the arc-jets ignitron power supply.

- that low magnitude fluctuations (1% of the dc component) with frequency components in the region of 10 to 120 kc were superimposed on the 180 cps variation. These fluctuations were random and their cause has not been determined. In calculating the stream velocity from the data, these fluctuations were separated from the signal components.
- that a high frequency component in the 1 to 5 megacycle region and of extremely low magnitude was present. This component of the signal is attributable to the noise in the photomultipliers. These fluctuations cannot be correlated or used to calculate the jet stream velocity.

Analysis of the signal characteristics indicates that the components of the signal which cannot be used for calculating the velocity must be removed without modifying the 10 to 120 kc component. Using such frequencies, the time difference between the two photomultiplier output signals ranges between two and six microseconds.

Three typical oscilloscope single sweep photographs of the photomultiplier output signals are presented in Fig. 5.3. The ac coupling of the scope removed the constant amplitude component and a 400 cps high pass filter removed the 180 cps component of the signal. The scope traces, therefore, contain only the random 10 to 120 kc signal and 1 to 5 megacycle noise.

Close analysis of the photographs in Fig. 5.3 reveal two undesirable limitations on this method of data recording; first, the high frequency noise makes exact determination of the location of peaks difficult and the errors encountered in measuring the distance between peaks can be large (for the velocity calculated from the data of Fig. 5.3c, an error of 0.5 microseconds corresponds to a calculated velocity error of approximately 7000 ft/sec. out of an estimated 50,000 ft/sec velocity). Second, due to the random occurrence of these fluctuations, many oscilloscope traces do not contain the 10 to 120 kc variations. Repeated experiments have shown an occurrence of approximately 50%.

5.3 *Preliminary signal correlation experiments*

Experimental procedure

Since the photographing of the signals displayed on an oscilloscope appeared to be inadequate for determining velocities a new method of data acquisition-reduction was investigated. In this approach, the two photomultiplier output signals were recorded on separate channels of a magnetic tape in the amplitude modulation mode and at a speed of 60 inches per second. This gave a maximum system recording frequency response of 120 kc. Thus, a large quantity of data was contained in each sample. By decreasing the tape speed upon playback to 1-7/8 inches per second and passing the signals through identical band pass filters into an analog signal correlator, a statistically-averaged phase shift for specific frequency bands of the two signals, was established. The stream velocity was then computed from the frequency and phase shift data by the relation

$$v = 3.60 \times 10^2 \frac{fd}{\theta}, \qquad (5.1)$$

where v = stream velocity (ft/sec),
d = entrance aperture separation (feet),
f = center frequency of frequency band (cycles/sec),
θ = measured phase angle (degrees).

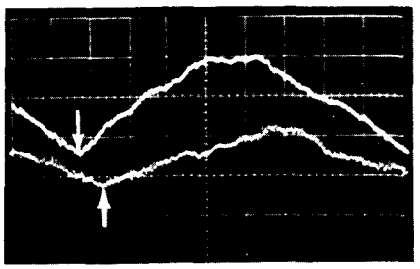

(a)

Conditions

a. Arc power	21.0 kw
b. Propellant flow rate	3.44×10^{-4} lb/sec
c. Exit enthalpy	59,000 B/lb
d. Chamber pressure	199 torr
e. Scope sweep rate	5 μsec/cm
f. Radial position	0.3 above axis
g. Calculated velocity	47,000 ft/sec

Description: Distortion due to presence of high frequency noise is shown. One minimum on this photograph enables a calculation of the velocity. Fluctuation frequency is 20 to 30 kc.

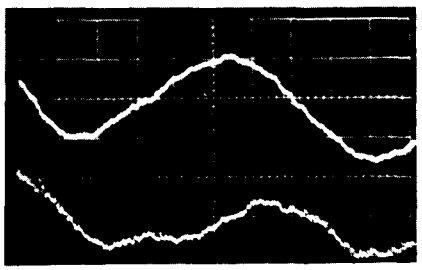

(b)

Conditions

a. Arc power	21.0 kw
b. Propellant flow rate	3.44×10^{-4} lb/sec
c. Exit enthalpy	59,000 B/lb
d. Chamber pressure	199 torr
e. Scope sweep rate	5 μsec/cm
f. Radial position	On axis

Description: No distinct maximum or minimum is present on this photo due to the presence of high frequency noise. The 20 to 30 kc signal is similar on both channels.

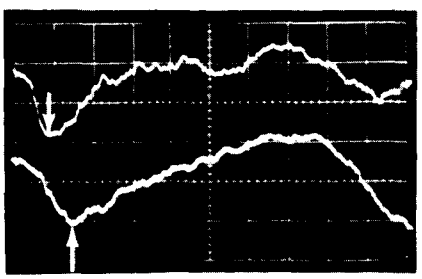

(c)

Conditions

a. Arc power	27.0 kw
b. Propellant flow rate	3.53×10^{-4} lb/sec
c. Exit enthalpy	72,500 B/lb
d. Chamber pressure	215 torr
e. Scope sweep rate	5 μsec/cm
f. Radial position	On axis
g. Calculated velocity	47,000 ft/sec

Description: High frequency noise is present but approximate velocity can be calculated from the minimum.

Fig. 5.3 Oscilloscope traces of velocity meter photomultiplier outputs

The signal correlation was accomplished by a McDonnell analog signal correlator with maximum response of 5 kc which necessitated the use of the tape speed reduction process. Correction was necessary in the data analysis for phase shifts attributable to the tape equipment and band pass filters.

The frequency range chosen to correlate the signals was 20 to 120 kc. This frequency range was divided into 8 frequency bands so that accurate phase angles at each center frequency could be established. The frequency bands were selected so that the ratio of center frequency to the bandwidth of the filters at each frequency band was approximately equal. The frequency bands and center frequencies before and after speed reduction are listed in Table 5.1.

Table 5.1 Data correlation frequency bands

Band number	Frequency band at 60 inches/sec	Center frequency	Frequency band at 1-7/8 inches/sec	Center frequency
	(kc)	(kc)	(cps)	(cps)
1	20–25	22.5	625–781	703
2	25–31	28	781–969	785
3	31–39	35	969–1219	1094
4	39–49	44	1219–1531	1375
5	49–61	55	1531–1906	1719
6	61–76	68.5	1906–2375	2141
7	76–95	85.5	2375–2969	2672
8	95–120	107.5	2969–3750	3359

The data were acquired by sighting the two velocity meter apertures along a plane at right angles to the nozzle exit plane with the upstream aperture sighted on the nozzle exit plane. The output signals of the photomultiplier tubes were recorded on tape for a period of 20 seconds at a tape speed of 60 inches per second so that a sufficient number of peaks could be statistically averaged. As shown by Fig. 5.4, the data acquisition system included the dual beam oscilloscope to monitor the taped signals.

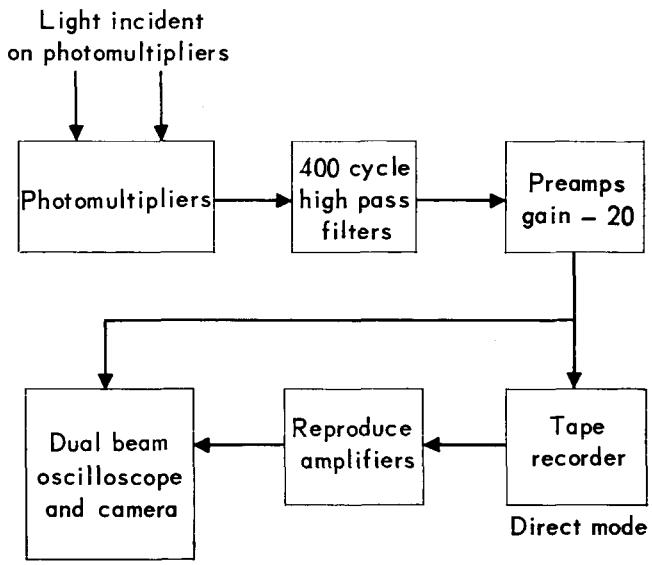

Fig. 5.4 Signal path for data acquisition

To reduce the data, the taped signals were reproduced through the equipment shown in Fig. 5.5. The analog signal correlator output represents the average cosine of the phase angle between the two input signals applied to the correlator. This was recorded on a strip chart. The stream velocity was then calculated by Eq. (5.1).

Aperture gap variation tests

Since the analog signal correlator output represents the average cosine of the phase angle between the two input signals, it is inherently insensitive to low phase angles. This places a lower limit on the distance between apertures for a given jet velocity. Also, an upper limit is imposed on the aperture separation distance due to the absence of signal similarity. In order to determine the aperture gap most suitable for measuring the jet velocities

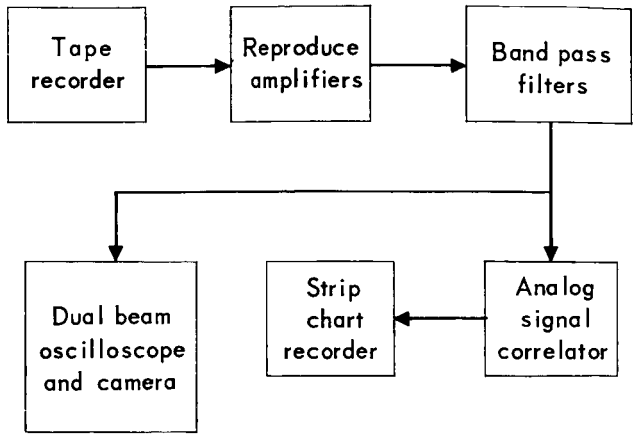

Fig. 5.5 Signal path for data reduction

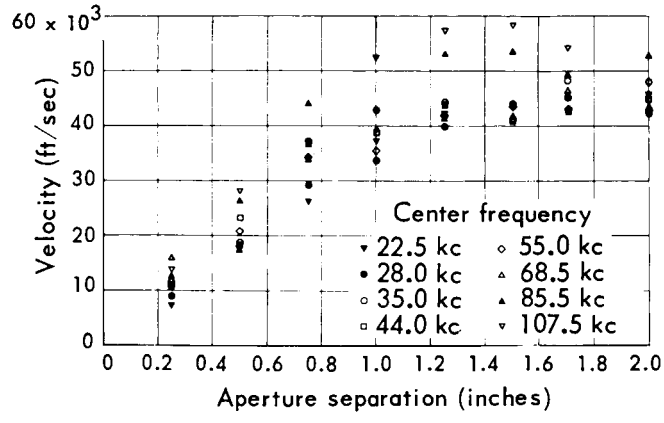

Fig. 5.6 Effect of aperture separation and signal frequency on velocity

under consideration, a series of tests were performed in which the aperture gap was varied from 0 to 2.0 inches in 0.25 inch steps. Mirrors were located in the optical path such that the apertures were aligned on the jet centerline. Data were recorded at each interval. The water-cooled 30 kw hydrogen arc-jet was stabilized at the bulk stagnation enthalpy level of 45,000 B/lb and data samples were recorded for each mirror position for 20 seconds. In addition, eight sine wave calibration signals were recorded to establish the phase shift attributable to the tape recorder and data reduction equipment.

The graphical results in Fig. 5.6 show that the scatter of data points at each aperture separation is appreciable and greater than desired, especially at the two higher frequency bands (center frequencies of 85.5 and 107.5 kc). Analysis of the results revealed that the accuracy of the velocities at separations below 1.0 inch was poor due to poor resolution at low phase angles. Also, poor signal correlation (signal similarity) at 2.0 inches gave unreliable velocities. However, the tests gave consistent and repeatable results for aperture gaps of 1.0 to 1.7 inches, the optimum being 1.5 to 1.7 inches.

The phase angle calibration results showed that the correction was small for signal frequencies up to 60 kc. It then increased to approximately 30^{o} at 100 kc.

Preliminary velocity profile tests

A series of experiments were performed to determine if a nozzle exit plane stream velocity profile could be established by the velocity meter using the signal correlation approach. For these tests the velocity meter was positioned so that the upstream phototube was sighted at the nozzle exit and the second phototube was positioned 1.7 inches downstream. The 30 kw water-cooled hydrogen arc-jet was stabilized at the bulk stagnation enthalpy level of 45,000 B/lb. Data samples were taken at 0.1 inch radial intervals from +0.7 to –0.7 inches off the nozzle axis. Each sample was 20 seconds in length. The gain of the system was not adjusted, making the signal level recorded on the tape higher near the center and lower near the edge of the jet. The calibration signal was recorded in the same manner as was done for the aperture gap variation tests.

The results showing the nozzle exit plane velocity profile are presented in Fig. 5.7. The data scatter for these tests is approximately ±15% in the region of the jet centerline. A frequency sensitivity is apparent. The large data scatter in the outer regions (beyond ± 0.5 inches) is attributable to the low signal amplitude in these data samples. The system signal gain was not adjusted for

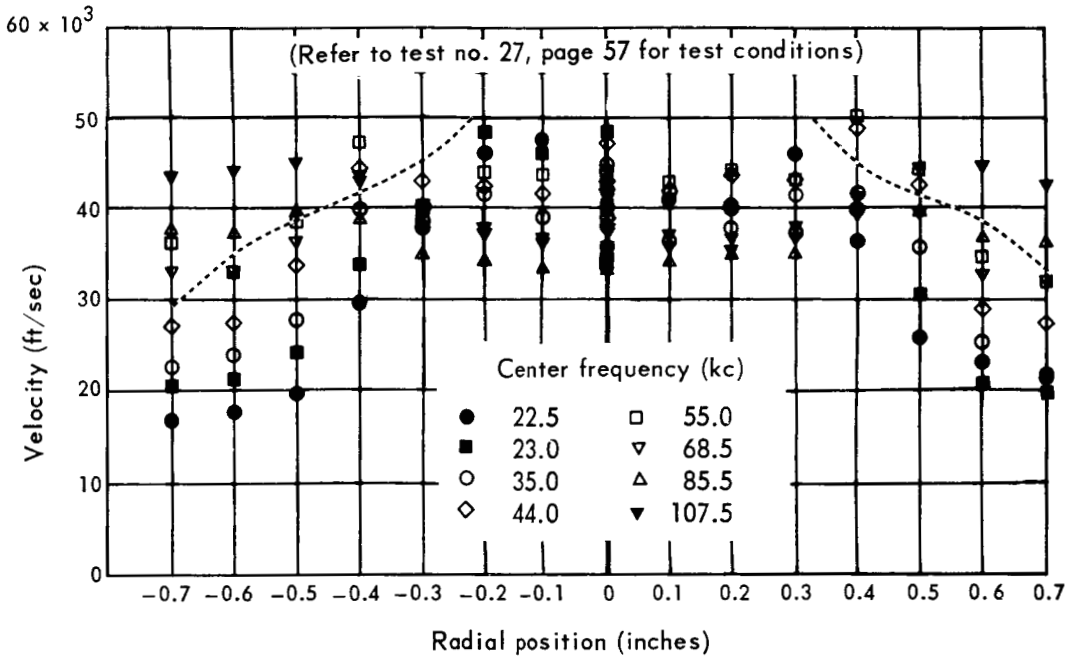

Fig. 5.7 Velocity meter data analysis by cross correlation

these tests. Thus, the data samples from the less luminous portions of the exhaust contained less signal. The analog signal correlator indicates approximately 90° phase shift (no correlation or random noise) for the data beyond 0.5 inches off the jet axis, especially at the higher frequencies. The data points below the dashed line in Fig. 5.7 are from data samples in which the signal strength was sufficient to provide a signal correlation.

A selenium full wave rectifier power supply was used to run the arc-jet for these tests and the photomultiplier output signals were monitored and photographed. Comparison of these signals with those made during the aperture gap variation tests using the ignitron half wave power supply showed no detectable deviation in signal character as a result of the change in the fundamental frequency and ripple content of the power supplied to the arc. It has been previously reported (Ref. 5.1) that the random fluctuations are caused by variations in the arc-jet power supply.

Photomultiplier frequency sensitivity tests

The frequency sensitivity of the preliminary velocity profile tests results could be attributable to the physical state of the exhaust or due to frequency sensitive velocity meter components. The recorded calibration signals indicated that the frequency sensitivity was not attributable to the tape recorder and data reduction apparatus. A bench test of the 400 cps high pass filters showed no significant phase shift of one filter with respect to the other from 10 to 120 kc. Therefore, the only remaining components which could cause phase shift were the photomultipliers. Therefore, a series of Kerr cell bench tests were performed to determine any "time of transit" differential of frequency sensitivity in the two phototubes.

To test these tubes, a Kerr cell equipped with the necessary polarizers was used as a high speed shutter and a standard tungsten lamp served as the light source. The experimental arrangement for these tests is shown in Fig. 5.8. Light fluctuation frequencies up to 60 kc were produced with this equipment. The alternating voltage which powered the Kerr cell was displayed on one beam of a dual beam oscilloscope and the photomultiplier output was displayed on the other beam. The Kerr cell shutter was operated in 10 kc steps from 20 to 60 kc. A phase relationship which

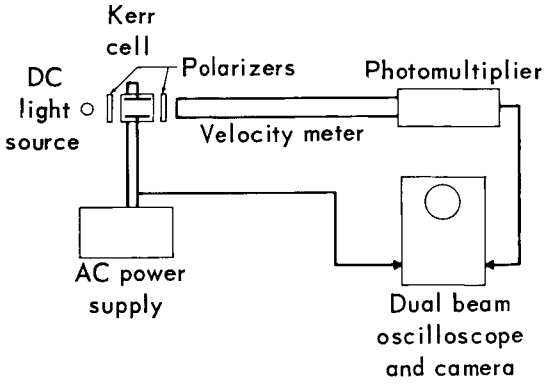

Fig. 5.8 Experimental apparatus for Kerr cell experiments

would be attributable to the photomultiplier could then be made from photographs of the oscilloscope single sweep traces obtained at each operating frequency. The procedure was identical in testing each photomultiplier.

The results showed that a 60^{o} phase shift existed in the photomultipliers at 40 kc. However, within a 5^{o} resolution, the phase shift in each tube at each frequency from 20 to 60 kc was identical. These results led to the conclusion that the frequency sensitivity observed in the velocity profile experiment was not attributable to the photomultipliers.

Tape recording tests

A series of experiments were performed to determine the repeatability and limits of accuracy of the tape recording process. Specifically, the purpose was to determine the repeatability of the magnitude and shape of the correlator output for a given data sample and, in addition, to determine if any phase shift existed as a function of location on the tape.

The procedure for the repeatability experiments was to record a 22.5 and a 107.5 kc sine wave and reproduce them through the band pass filters into the analog signal correlator over a period of several days (traversing through them a total of 10 times). On a separate tape, 20, 40 and 60 kc sine wave data samples were recorded for a period of 20 seconds each at the beginning, center, and end of the tape reel.

The results of these tests indicated that non-systematic errors are inherent in the signal tape recording process, but that they are not sufficient in magnitude to account for the large data scatter observed in the preliminary velocity profile experiments. The reproducibility of a single data sample was within $\pm 3^{o}$ at 22.5 and $\pm 7^{o}$ at 107.5 kc for the 10 traversals. Considering the effect of position on the tape, typical results showed a $\pm 7^{o}$ error at 20 kc. These errors cannot be eliminated by calibration because they are not systematic and thus, an estimated 5% uncertainty is introduced in the calculated velocity due to the signal tape recording process.

5.4 *Velocity profile measurements*

Further analyses of the preliminary signal correlation experimental procedures and results indicated that two possible improvements could be made. The first was to provide the velocity meter with an angular adjustment so that each data sample would be taken along a stream line. One aperture was sighted at the nozzle exit plane and the other 1.7 inches downstream. Thus, for the centerline sample only, a line which would connect the apertures would be perpendicular to the nozzle exit plane. In the previous tests, the line between the two apertures was always parallel to the jet axis. The second improvement involved adjustment of the photomultiplier gains so that a 1.0 volt rms signal strength was recorded on the tape for each sample.

Two series of tests were performed; one at a bulk stagnation enthalpy level of 45,000 B/lb (Fig. 5.9) and another at 60,000 B/lb. Data samples were recorded at 0.10 inch radial intervals traversing

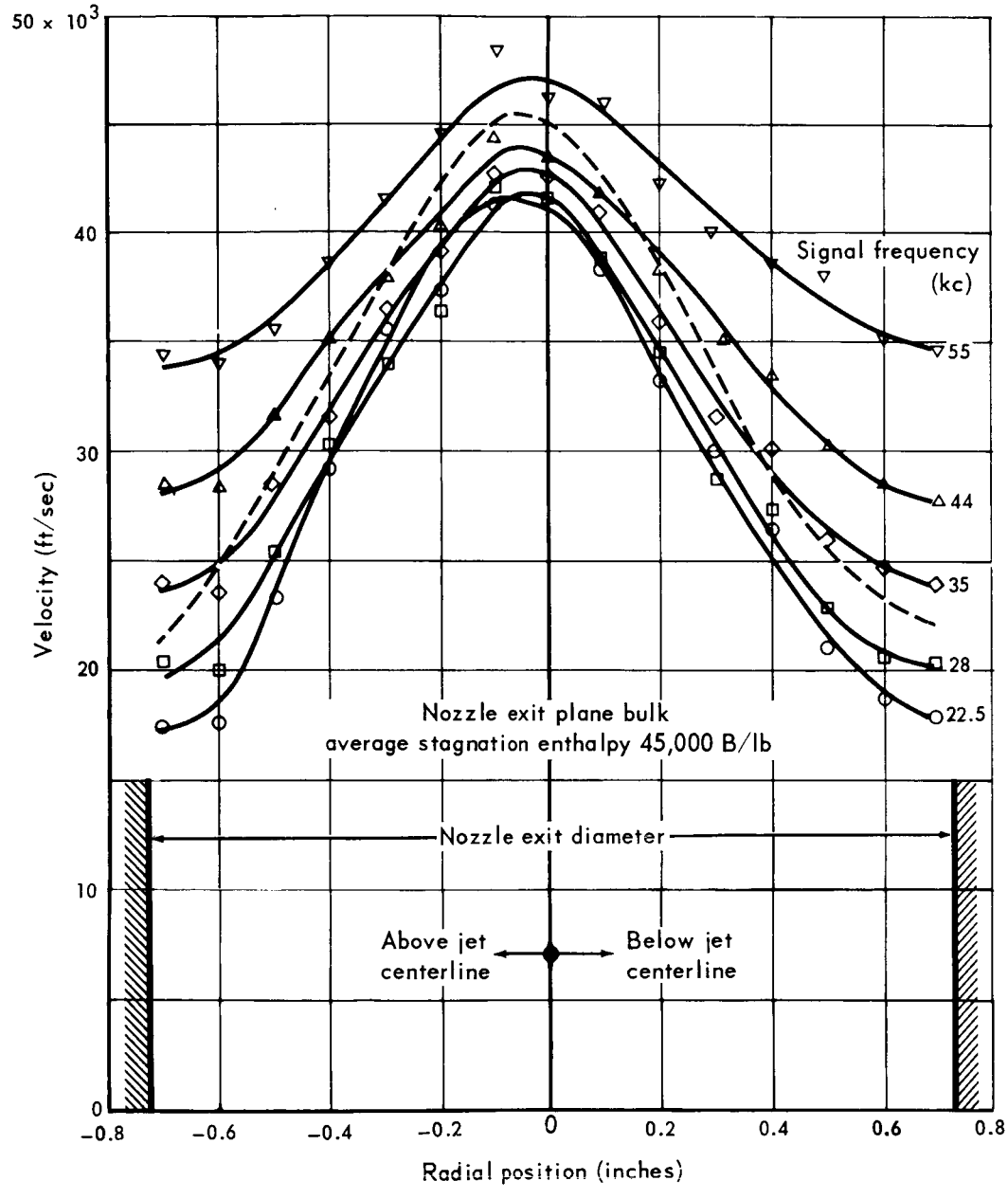

Fig. 5.9 Velocity meter profile by cross correlation

the nozzle exit plane vertically from +0.7 to -0.7 inches. The results of the velocity profile measurements for the 45,000 B/lb enthalpy tests are shown in Fig. 5.9. The signal strength in the upper 3 frequency bands was less than the 0.10 volt rms required for the signal correlator. Therefore, only the data for the 5 lower frequency bands are presented.

The frequency sensitivity characteristics of the velocity profile measurements are apparent in Fig. 5.9. The measurements near the edge of the jet are more sensitive to frequency than those nearer the jet centerline. It is observed that the peak velocity occurs below the jet centerline.

The data scatter is attributed – at least in part – to the dark current noise which is present in the photomultiplier output even when no light is striking the photosensitive cathode. Although a quantative analysis is lacking, it is evident that the data scatter is less for high signal to noise ratios. The signal strength is lower at the higher frequencies and lower at the edge of the jet because of the low luminosity in this region. Hence, the data scatter is greater for those conditions as shown on the graph.

If a minimum signal strength of 0.15 volts rms is used as a criterion for the acceptance of data points, the data scatter is reduced to approximately ±5% for all data within ±0.5 inches of the jet axis. The data points below the dotted line in Fig. 5.9 represent signal strengths greater than 0.15 volts rms.

These velocity profile measurements at the low bulk stagnation enthalpy conditions (45,000 B/lb) appear to be valid. The shape of the profiles are reasonable in that they peak near the jet centerline and decrease to the jet boundary. Energy balance calculations and comparison with the thrust measurements also indicate that the magnitude of the velocities are reasonable.

The velocity profile tests at the 60,000 B/lb enthalpy level showed a larger scatter of data than the 45,000 B/lb tests and the effects of signal frequency were more severe. The results at all frequency bands showed that the peak velocity occurred 0.30 inches above the jet centerline. The magnitude of the phase shift of specific frequency bands at each exhaust position did not necessarily repeat.

It should be reiterated that the determination of arc-jet velocities by this approach assumes that the random fluctuations travel at the stream aerodynamic velocity. At present, the nature of these fluctuations are not known, but the assumption appears valid for an arc-jet exhausting into a vacuum. However, Freeman and Li (Ref. 5.2) observed that the natural fluctuations existing in an arc-jet exhausting into an ambient atmospheric pressure contained components which did not travel at the stream velocity.

To investigate the frequency distribution of the random fluctuations as a function of position across the exhaust, two samples from the 45,000 B/lb tests were re-recorded and a power spectral density analysis was performed. The samples included one from the jet centerline and one 0.5 inches off the centerline. The results are shown

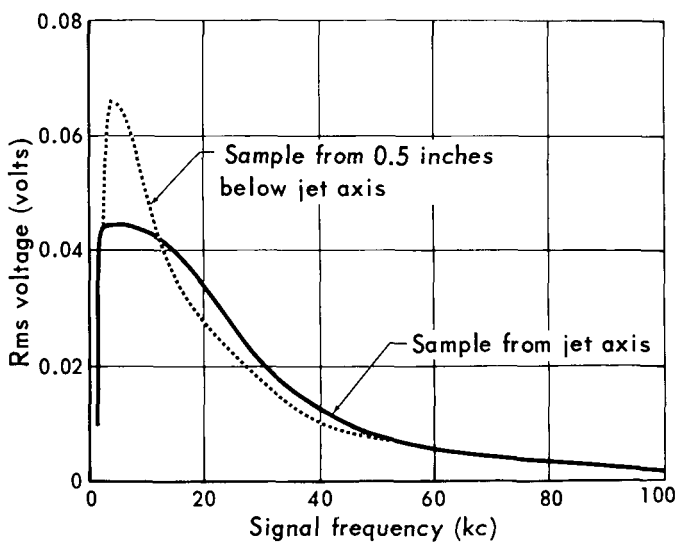

Fig. 5.10 Power spectral density of fluctuations emitted from hydrogen exhaust

in Fig. 5.10. It appears that most of the signal energy is below 40 kc and that the lower frequencies predominate in the sample off the jet centerline.

5.5 High frequency correlator

The previous test results show the necessity of reducing the frequency sensitive data characteristics and demonstrate a need for determining the validity of the calculated velocities from the velocity meter data. Also, as borne out by previous experiments, the recording of the photomultiplier output signals on tape has introduced an uncertainty in the results and has required a difficult and lengthy data reduction procedure.

The design of a special high frequency analog signal correlator which would reduce the effects of the above difficulties was initiated. By extending the frequency response to 100 kc, the necessity of taping the signals would be eliminated.

Inclusion of a continuously variable delay line in the phase leading input would enable performance of signal cross correlation which is independent of signal coherence. It appears that the frequency sensitivity of the velocity measurements illustrated in the previous tests is caused by the operation of the correlator with partially dissimilar signals in the cos θ mode. As the rms signal voltages decrease, the effects of incoherent noise become significant and thereby, the correlator gives a resultant calculated velocity which would tend to be higher than actual. By measuring the required time to bring the two input signals into phase by means of the delay line in the cross correlate operating mode, the deleterious effects of signal dissimilarity are eliminated.

The degree of signal similarity would aid in determining the validity of the calculated velocities from the velocity meter data. The velocity meter does not "see" a point in the plasma, but rather, "sees" a cross-section through the plasma. Thus, contributions due to fluctuations which are not in the region of the point will be present in the photomultiplier outputs. If the radial dimensions of the intensity distrubances are large relative to the nozzle diameter, the integrated intensity observed by sighting through the exhaust should change the character of the signal at each phototube. This being the case, the signals would not correlate. Therefore, the criterion which is acceptable for determining a velocity from the velocity meter data is the proof of similar signals. This proof can be established by an auto-correlation cross-correlation process described in the following paragraphs.

The special high frequency correlator was designed to the following specifications:

- signal correlation capability from 1,000 to 100,000 cps;
- correlation frequencies to be limited in a specific data sample by means of band pass filters;
- the correlator to have the following operating modes: auto-correlate, cross-correlate, and cos θ;
- a variable time delay in one channel from 0.5 microsecond to 12 microseconds with 0.1 microsecond resolution;
- measureable rms voltage levels of the filtered photomultiplier outputs.

Tests with the high frequency correlator and the hydrogen arc-jets have not yet begun. It is anticipated that the tests will be performed with the hydrogen arc-jets in the following manner.

In operation, the frequencies at which natural random fluctuations are observed are divided into bands. The selection of these bands are made with the variable band pass filters. With the arc-jet operating and the correlator switched to the cross-correlate mode, the rms level of each filtered photomultiplier output is adjusted so that

the signal strengths applied to the correlator inputs are equal. The delay line is switched into the phase leading input until the correlator output passes through a maximum. This procedure will define a curve which mathematically may be expressed as

$$R_{xy} = \frac{1}{2T}\int_{-T}^{T} x(t)\ y\ (t + \tau)\ dt$$

where R_{xy} = cross-correlation function,
$x(t)$ = phase lagging signal,
$y(t)$ = phase leading signal,
τ = time delay

A typical curve defined by this process is shown in Fig. 5.11. As the two signals x(t) and y(t) are brought "in-phase" by varying τ, R_{xy} will pass through a maximum. This value is designated as τ_o on the graph. The above procedure is repeated for all frequency bands in which the spectral density is sufficient to give at least a minimum signal strength at the correlator inputs.

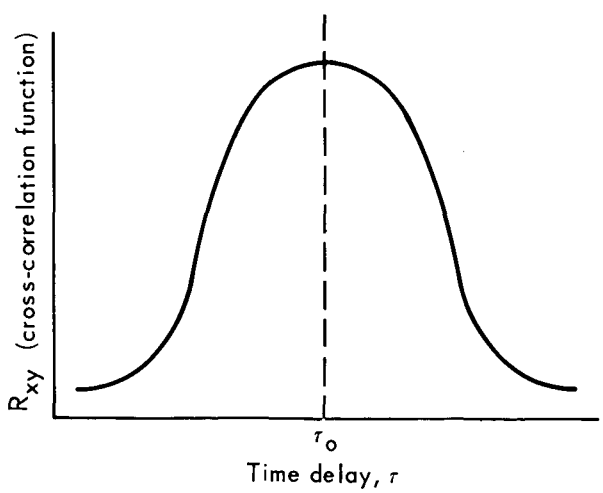

Fig. 5.11 Cross correlation function versus delay time

Upon completion of the correlation process, an auto-correlation is accomplished with the upstream photomultiplier output. The auto-correlation is performed in the same frequency band at which the cross-correlation output was maximum. In this function, mathematically the following is performed:

$$R_{xx} = \frac{1}{2T}\int_{-T}^{T} x(t)\ x\ (t + \tau)\ dt$$

where R_{xx} = auto-correlation function,
$x(t)$ = signal applied to both correlator inputs,
τ = time delay.

A typical curve defined by this process is shown in Fig. 5.12. In auto-correlating, the signals are

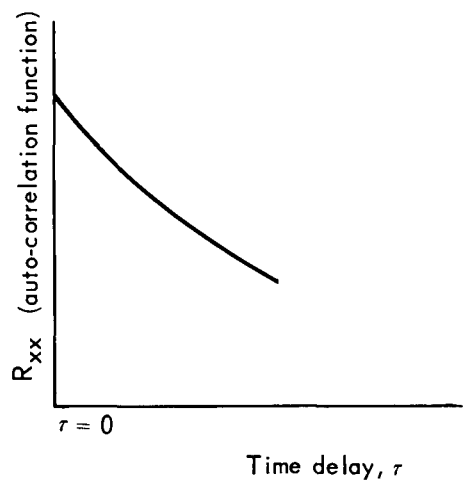

Fig. 5.12 Auto correlation function versus delay time

"in-phase" at $\tau = 0$ and therefore R_{xx} is maximum at $\tau = 0$. As τ is increased from 0, the magnitude of R_{xx} decreases. Together, the auto-correlation and cross-correlation functions will give an index of signal similarity which is a definite indicator of the validity of the velocity computed from the data. This index of signal similarity is defined by

$$I = \frac{R_{xy}\ (\tau = \tau_o)}{R_{xx}\ (\tau = 0)}$$

The frequency band which gives the highest signal similarity index is used to obtain data from which velocity calculations are made.

There are two methods of obtaining the velocity from the data. First, it may be obtained from

$$v\ (ft/sec) = 0.15/\tau_0,$$

where τ_0 = time delay when R_{xy} is a maximum. Or, the correlator may be switched to the cos θ mode and its output displayed on a strip chart recorder. The plasma stream velocity is then computed from

$$v\ (ft/sec) = 51 f_0\ /\theta,$$

where f_0 = band center frequency (cycles/sec),
θ = measured phase angle (degrees).
The method which gives the best resolution will be used.

Photometric velocity meter observations of the arc region are planned to investigate the nature and cause of the random light fluctuations. They may be inherent in the arc processes; they may be caused by arc-electrode attachment and detachment; or other reasons may account for their presence.

It is also planned to "pulse" the plasma stream by means of a spark discharge or similar technique and determine the exhaust stream velocity by means of the velocity meter. These results will then be compared with those obtained by the present technique using the inherent light fluctuations.

5.6 Conclusions

The results of the photometric velocity experiments indicate:

1. The present velocity measurements are sensitive to the signal frequency.
2. The recording of the photomultiplier output signals on tape introduced an uncertainty in the results.
3. A need exists for determining the validity of the calculated velocities from the velocity meter data.
4. A high frequency correlator should alleviate the frequency sensitivity and taping problems and determine the validity of the velocities calculated from the velocity meter data.

References

5.1 *E. C. Winkler and R. M. Griffin Jr., "Effects of Surface Recombination on Heat Transfer to Bodies in a High Enthalpy Stream of Partially Dissociated Nitrogen," NASA TN D-1146 (Dec. 1961).*

5.2 *M. P. Freeman and S. U. Li, "Velocity of Propagation and Nature of Luminosity Fluctuations in a Plasma Jet," J. of Appl. Physics Vol. 33, No. 9, (Dec. 1962).*

6 Electron beam

The feasibility of using an electron beam as a density probe for measurements in rarefied gas flows has been successfully demonstrated by Hurlbut (Ref. 6.1). However, the feasibility of using this technique to measure density distributions in a hydrogen arc-jet exhaust where the static pressure is an order of magnitude greater than that in Hurlbut's work, has not been successfully demonstrated.

The purpose of the electron beam experiments described herein was to apply this technique, if possible, to density measurements in a hydrogen arc-jet exhaust.

6.1 Theoretical considerations

The expression required to deduce the density distribution of an axisymmetric jet from measurements of beam transmission is presented in Ref. 1.1 In that analysis the beam originates at a point and is moved through an angle which allows it to traverse the cylindrical exhaust from the centerline to its maximum diameter. If the beam traverses the exhaust in a direction always normal to a single vertical plane through the axis of the exhaust as in Fig. 6.1, the applicable expression is:

$$n(r) - n_1 = \frac{1}{\pi Q} \int_r^R \frac{d}{dy}\left[\ln\left(\frac{I(y)}{I_o}\right)\right] \frac{dy}{(y^2 - r^2)^{1/2}} \quad , (6.1)$$

where $n(r)$ = number density in the exhaust,

n_1 = number density in the region surrounding the exhaust,

Q = total electron scattering cross section.

The other quantities are defined in Fig. 6.1.

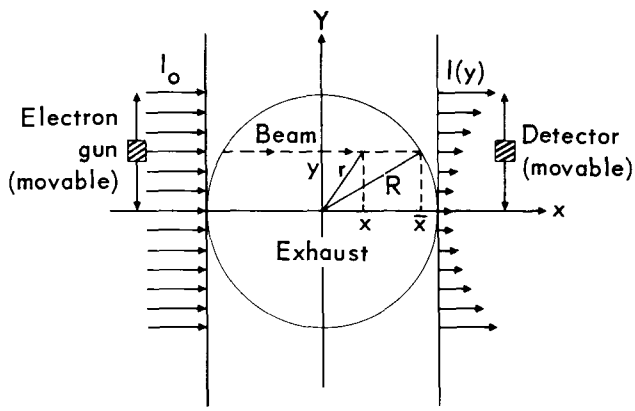

Fig. 6.1 Diagram for explanation of electron beam attenuation theory

In order to obtain an estimate of the accuracy with which the ratio $I(y)/I_o$ must be measured to yield meaningful density profiles, it was decided to analytically determine the transmission ratios in an axisymmetric exhaust assuming various temperature distributions across the jet. Figure 6.2

depicts the arc-jet exhaust model used for these computations. The following assumptions were made:

- The distance between the electron emitter and collector perpendicular to the exhaust centerline is 5 inches.
- The exhaust exit plane diameter is 2 inches (R = 1).
- The exit plane pressure (exhaust static pressure) is 2 torr and constant across the nozzle exit plane.
- The temperature decreases parabolically from the jet centerline to 2,000°K at R_o.
- The region surrounding the jet is at a temperature of 2,000°K and a pressure of 0.2 torr.

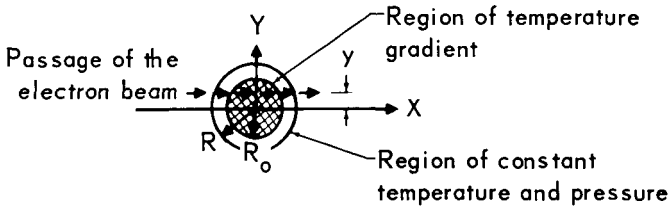

Fig. 6.2 Cross section of arc-jet exhaust

The results of the calculations for several axis temperatures are shown in Figs. 6.3 and 6.4. In Fig. 6.3 the temperature distribution is peaked about the centerline, and in Fig. 6.4 the temperature gradient extends over the entire diameter of the jet exhaust.

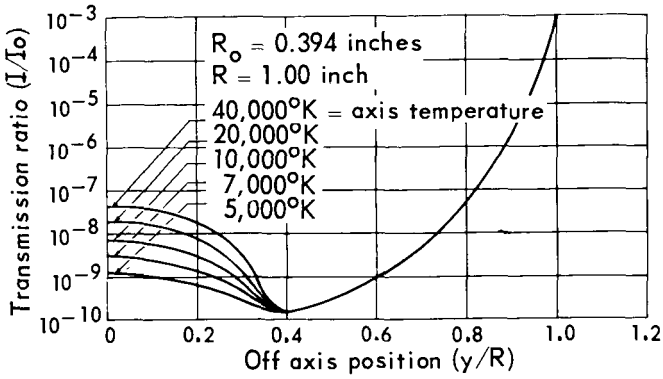

Fig. 6.3 Calculated transmittance ratio as a function of off axis position

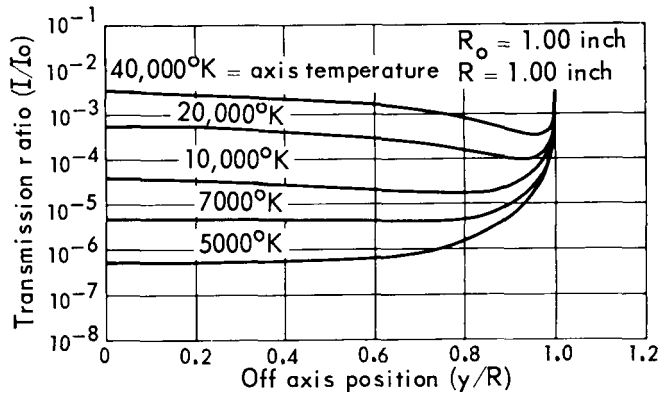

Fig. 6.4 Calculated transmittance ratio as a function of off axis position

6.2 *Development of apparatus*

The electron beam apparatus used in the original tests on the arc-jet exhaust is shown schematically in Fig. 6.5. The significant features of this apparatus are that the collector has a solid angle cone of acceptance of approximately 2π, thus allowing scattered electrons to reach the collector. Also the apparatus provides no means of measuring the beam current entering the gas.

In tests conducted on an arc-jet exhaust with this apparatus, a large background current was

observed at the collector. This was attributed to the ionized gas of the exhaust plume. It was decided that tests should be run in gases at room temperature to determine the validity of the hard sphere scattering model assumed in the derivation of Eq (6.1) and also to develop components that might be incorporated into the final apparatus.

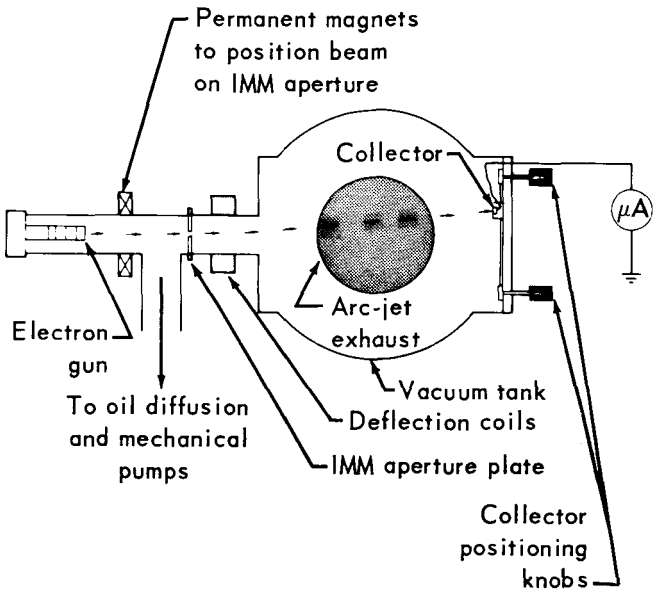

Fig. 6.5 Schematic diagram of original electron beam apparatus

A schematic diagram of the first cold gas apparatus is shown in Fig. 6.6. The electron gun, a commercial type, is shown schematically in Fig. 6.7. The gun is focused electrostatically and control of the potential of the various electrodes is provided by the voltage dividing network shown in the circuit diagram of Fig. 6.8. It will be noted that instead of the cathode being at ground potential and the anode at a high positive potential (10^4 volts) as is normally the case, the cathode is maintained at 10^4 volts negative and the anode is at ground potential. One reason for this is that the field established between the vacuum tank on which the arc-jet is mounted and a high potential anode would tend to diffuse the beam. In addition, problems of arcing between the anode and the vacuum tank might appear.

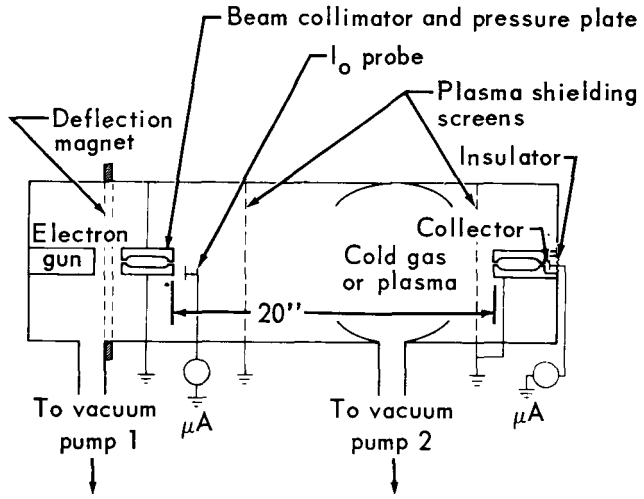

Fig. 6.6 Schematic diagram of electron beam apparatus

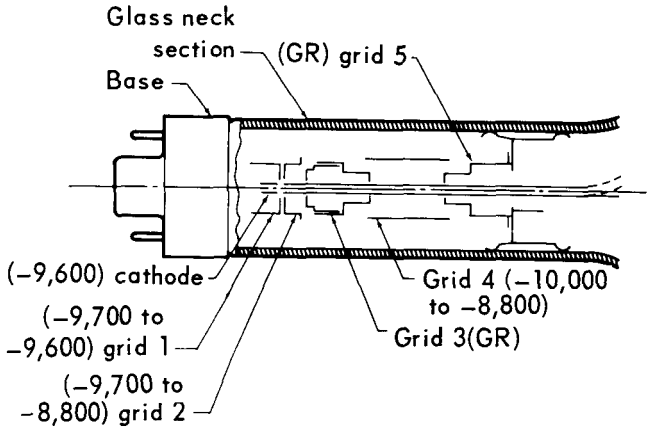

Fig. 6.7 Schematic diagram of electron gun

To provide a stable, low pressure atmosphere for the electron gun, a plate containing a 0.010 inch diameter hole is located between the gun cavity and the region containing the gas to be studied. With this size hole a pressure of 8×10^{-4} torr can be maintained in the gun region. The beam from the electron gun is directed through the

beam collimator aperture by means of permanent magnets surrounding the gun cavity. This magnet is adjusted mechanically. If the gun is not located in its cavity so that only a small deflection is required to pass to beam through the aperture, a diffusion of the beam occurs.

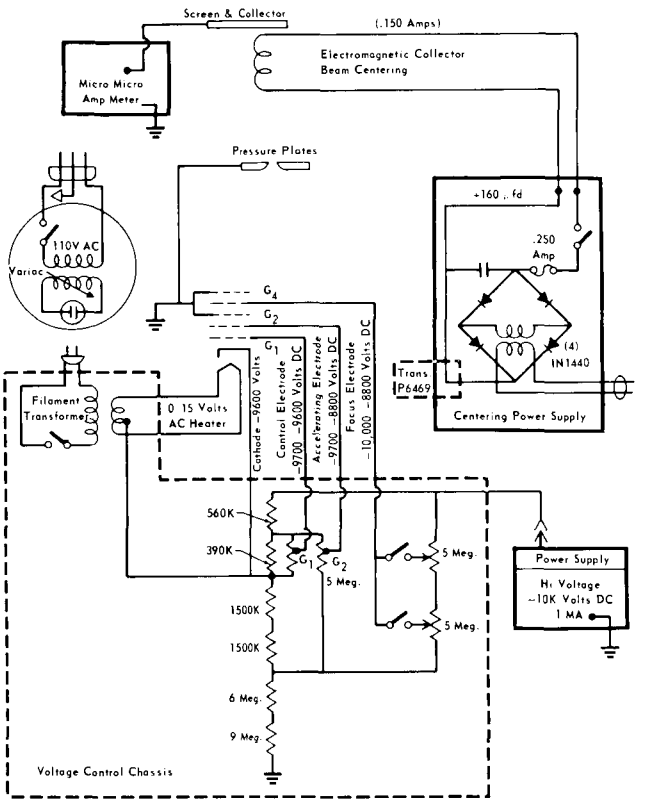

Fig. 6.8 Electron beam power supplies

After the beam is passed through the aperture separating the gun region from the test region, a probe is used to measure the unattenuated beam current, I_o. This probe consists of a Plexiglas arm which holds a brass collector which – in turn – is connected to the microammeter by an insulated wire. A mechanical linkage is provided to move the probe into the beam.

The plasma shielding screens are grounded when cold gas is being studied and serve only to carry off electrons scattered from the beam. When a plasma attenuates the beam, a negative potential must be applied to the screens. This potential barrier serves to shield the probe and the collector from the plasma.

The final collector assembly consists of a collimator and the collector itself. The collimator defines the cone of acceptance of the collector and contains two 0.031 inch diameter holes four inches apart. The collector is located immediately behind the last of these holes and is insulated from the collimating section. The collecting section can be replaced with a Plexiglas window coated with a phosphor compound to aid in alignment of the apparatus.

Several tests were performed in hydrogen, helium, and argon using the system shown in Fig. 6.6 without a collimator at the final collector. In making these measurements, the pressure in the gas region was adjusted to a predetermined value; the probe was inserted to measure the beam current entering the test section; the probe was retracted and the final collector assembly was used to measure the unscattered beam current passing through the gas.

Figure 6.9 shows the results of these tests in which the values of I_o were repeated for three consecutive measurements.

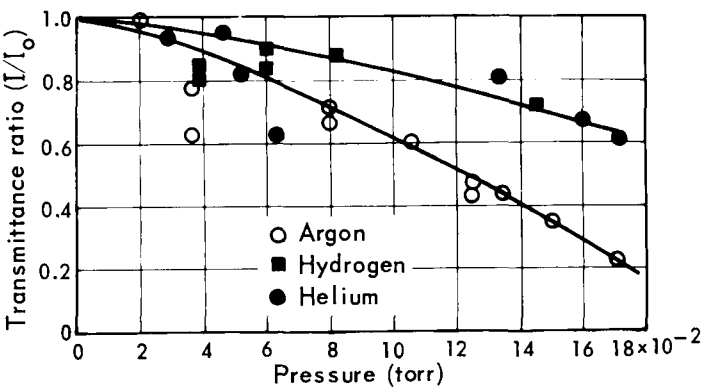

Fig. 6.9 Electron beam cold gas transmittance

In using the apparatus to perform these cold gas density tests, it became evident that several modifications were necessary. Specifically, a more stable low pressure environment was required for the electron gun; greater flexibility was desirable in the alignment of the components and apertures; and it was necessary to decrease the distortion of the electron beam by the positioning devices and apertures.

The electron beam system was modified as shown in Fig. 6.10. The aperture in the plate seperating the test section from the gun cavity was reduced from 0.010 inch diameter to 0.004 inch diameter and the capacity of the mechanical pumping system attached to the oil diffusion pump was increased. All apertures were fabricated from nickel instead of the aluminum originally used in order to reduce the amount of corrosion produced by electron bombardment. With these changes, a pressure of 10^{-5} torr could be maintained in the region of the electron gun.

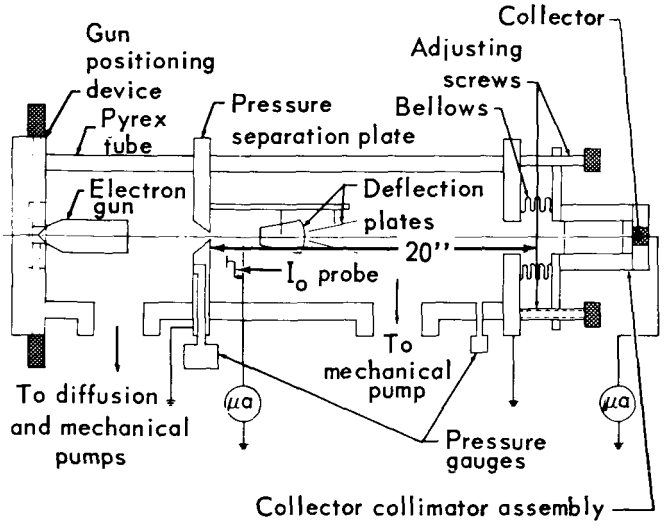

Fig. 6.10 Schematic diagram of electron beam apparatus

To provide greater alignment flexibility, an assembly was added which allowed the axis of the collector to be aligned with the electron beam. This assembly consists of a bellows for attaching the collector to the vacuum system. A universal joint provides freedom of motion of this assembly. The collector assembly is aligned by adjusting the set screws shown in Fig. 6.10. For positioning the electron beam on the initial collector aperture, electrostatic deflection plates were added external to the electron gun cavity. Addition of these plates necessitated changes in the voltage dividing network. The revised circuitry is shown in Fig. 6.11. The deflection plates produced less distortion of the beam than did the electromagnetic coil previously used. To decrease the distortion of the beam incident on the aperture enclosing the gun cavity, the permanent magnets were replaced by a mechanical device which allows the gun itself to be aligned with the aperture.

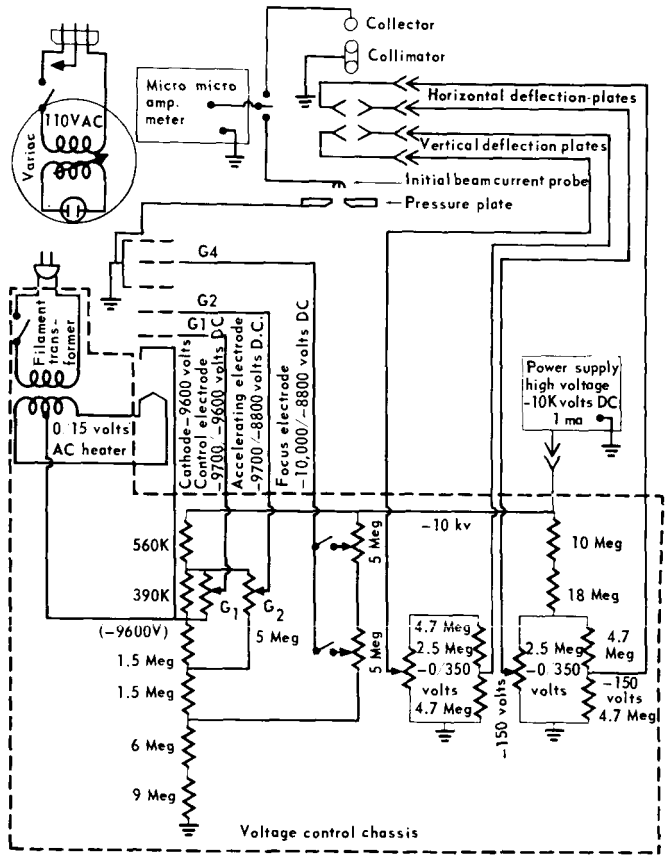

Fig. 6.11 Electron beam device with power supply

The revised system was successfully aligned and used to obtain the cold gas hydrogen data shown in Fig. 6.12. The initial beam current I_o was decreased to 5 microamperes in order to reduce spreading of the beam from space charge repulsion. The beam current, I, observed at the collector was corrected to account for such spreading. An initial beam current of 5 microamperes was chosen because this current could readily be reproduced.

The procedure followed in obtaining the data was to set the hydrogen pressure in the test section and measure the value of I_o with the probe. The probe was then removed and the value of I measured. The probe was then reinserted to check the value of I_o.

It can be seen from Fig. 6.12 that the ratio I/I_o is reproducible within a factor of four for 4 of the 5 tests. The data of run 3 is not consistent with the other 4 runs. The discrepancy is thought to be due to misalignment.

Without three degrees of freedom in the alignment of the collector, no beam current could be measured. It was found that beam alignment was very sensitive to vibration and to minute changes in the position of the collector. To obtain each data point, the system was aligned to produce a maximum beam current at the collector. The apparatus contains O-rings and a single rigid bellows which are believed to compress or expand slightly with variation of test section pressure. These slight distortions appeared to be sufficient to cause misalignment of the collector system. Slight changes in test section pressure reduced the collector current to zero if a realignment of the collector was not attempted.

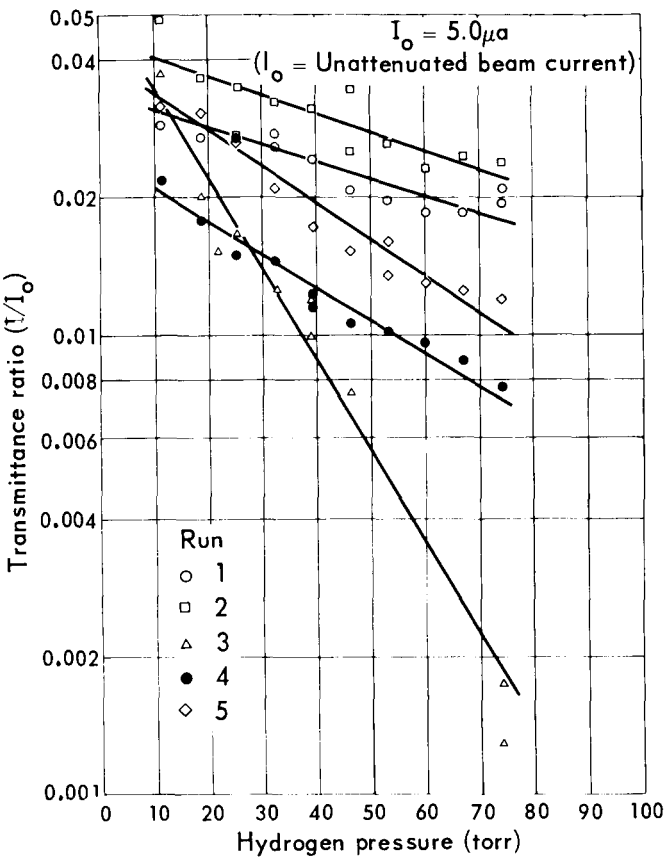

Fig. 6.12 Transmittance ratio I/I_o as a function of hydrogen pressure

6.3 *Discussion of results*

The results of the above experiments indicate that the transmission ratio was reproduced within a factor of four for four of the tests. These results were obtained with 5.0 μa as the initial beam current I_o, resulting in measured transmission ratios of the order of 1×10^{-2} to 5×10^{-2}.

In order to establish whether or not the present electron beam characteristics are ammendable to measuring arc-jet density profiles, it is necessary to compare the experimental results with the analytical predictions of the transmission ratios. It should be noted that the assumed temperature profiles for these calculations are thought to be rather extreme. Hence, it is felt that the calcul-

ated transmittance ratios represent minimum levels which must be achieved with the experimental apparatus.

Consider the two cases illustrated graphically in Figs. 6.4 and 6.5. Figure 6.4 depicts the transmission ratio versus off-axis position characteristics for several parabolic temperature distributions decreasing to 2000°K at R_o = 0.394 inches (Fig. 6.2). For this case the gradient of the transmittance ratio (which is required to obtain the number density) is sufficiently large that an error of a factor of four would yield an approximate value of the number density. However, the transmittance ratios required (10^{-7} to 10^{-9}) are five orders of magnitude lower than have been achieved using the present apparatus.

Figure 6.5 presents the characteristics for several parabolic temperature distributions decreasing to 2000°K at R_o = 1.00 inches. For this case the gradient of I/I_o is too small to be detected with the present equipment and transmittance ratios required (10^{-3} to 10^{-7}) are still below the range of the present equipment.

As a result of these comparisons it appears that the present apparatus does not possess sufficient sensitivity and the necessary reproducibility required to obtain meaningful density profiles in a hydrogen arc-jet exhaust whose exit plane pressure is 2 torr. The reproducibility of the apparatus could be improved by more accurate alignment of the electron beam components. However, in view of the necessity of traversing the exhaust plume, the time required to obtain an accurate alignment could prove prohibitive. In addition, the inherent vibration of the vacuum system further complicates the alignment problem.

The ability to measure transmittance ratios in the range of 10^{-5} to 10^{-7} would require an improvement of a factor of approximately 10^4. This could possibly be attained by raising I_o by this factor. However, an additional problem of beam focusing would be encountered.

Reference

6.1 F.C. Hurlbut, "Electron Beam Density Probe for Measurements in Rarefied Gas Flows," J. Appl. Phys. 30, 273 (1959).

7 Langmuir probe

The object of this program was to investigate the use of single Langmuir probes for measuring the electron densities at different axial and radial positions in the exhaust of a 30 kw hydrogen arc-jet.

Reference 1.1 presents the theory and experimental results obtained using single and double Langmuir probes in the exhaust of a 30 kw hydrogen arc-jet. The process of data analysis and reduction are also described in that report.

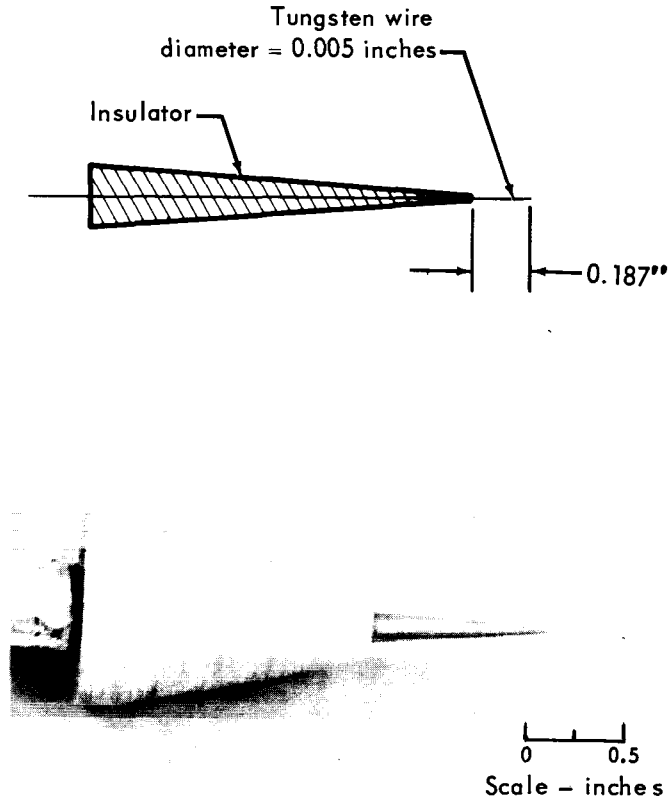

Fig. 7.1 Langmuir probe

7.1 Experimental apparatus

An analysis of the results of the Langmuir probe work described in Ref. 1.1 suggested several improvements in the experimental apparatus. A probe holder having a better aerodynamic configuration was designed to eliminate possible interferring shocks (Fig. 7.1). Provisions for obtaining radial and axial profiles were incorporated in the positioning mechanism. Also the Langmuir probe circuit was redesigned (Fig. 7.2) so as to better balance out the circuit noise and to provide means for recording data on tape and oscilloscope rather than on oscilloscope alone.

The probe (Fig. 7.1) consists of a tungsten wire insulated by a ceramic. The insulator is used to cover all but the tip of the wire so that the surface area of the collector is defined.

The actuator system (Fig. 7.3) was fabricated to sweep the probe rapidly through the arc-jet exhaust in order to prevent excessive probe damage due to the high incident heat flux. A device to sweep the probe through selected planes perpendicular to the jet axis was also constructed and is shown in this photograph.

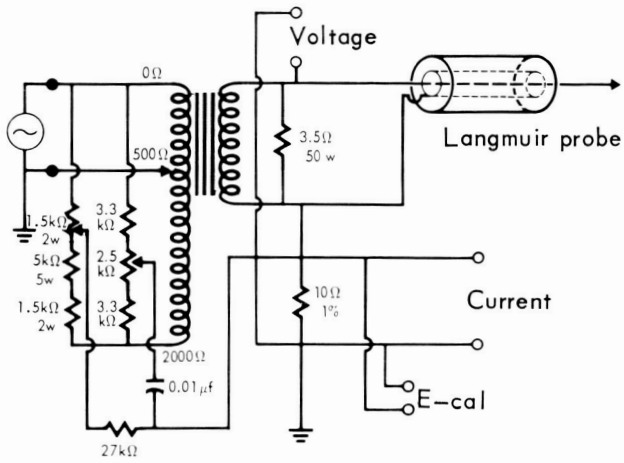

Fig. 7.2 Langmuir probe circuit

Figure 7.4 shows the two techniques used to record the probe voltage and current. The data recorded on the tape system is used for primary data reduction, and the oscilloscope photographs are used as a check.

The power input for the circuit was supplied by a power amplifier, whose output was taken from two 4 x 150–A tubes. The signal for the power amplifier was supplied by a 200 AB signal generator. The voltage and current were recorded on magnetic tape through a fourteen channel tape recorder operated at 60 inches/sec using a fm recorder amplifier. Also, the voltage and current were photographed on the oscilloscope.

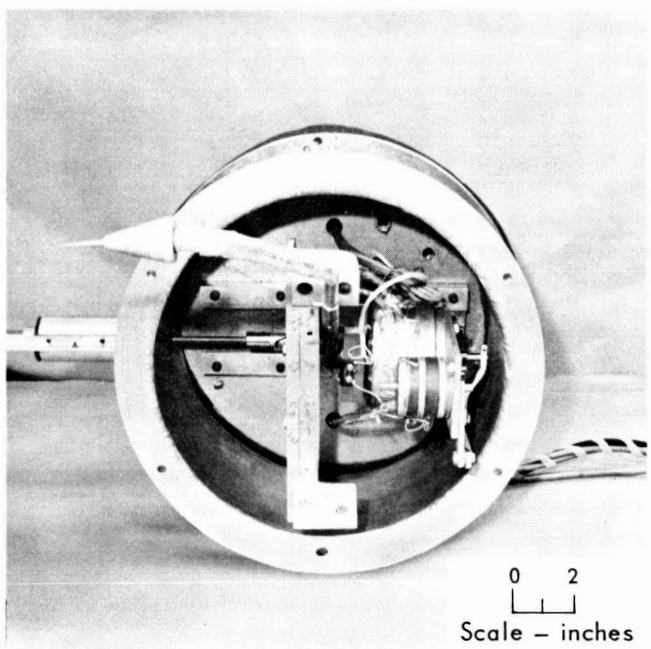

Fig. 7.3 Langmuir probe axial position measuring device and actuator system

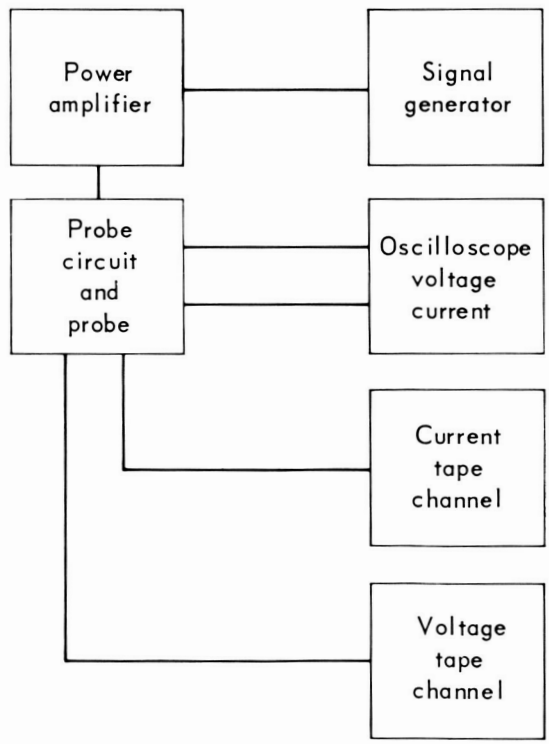

Fig. 7.4 Langmuir probe instrumentation

7.2 Preliminary tests

The signal voltage was attenuated before it was recorded. The voltage, set by a 400 AB rms vacuum tube voltmeter, was noted and recorded. A calibrated voltage (±2%) source was applied accross a 10 ohm 1% resistor to provide a current calibration. The current and its calibration were recorded and prior to the test, the circuit was balanced. The probe voltage and current were recorded on tape as the probe was swept as a pendulum through the hydrogen arc-jet exhaust and back again in a period of approximately one second. A separate resistance circuit relates the position of the probe in the jet to its angular deflection.

The initial tests at a bulk stagnation enthalpy level of 45,000 B/lb resulted in a breakdown of the insulating material between the probe and its holder and in excessive heating of the motor sweeping the probe through the plasma. These difficulties were eliminated and further tests were performed at the same arc-jet operating conditions. The electron densities calculated from these tests ranged from 2.6×10^{11} to 5.8×10^{11} electrons/cm^3.

These values are in the range expected based on energy balance calculations assuming frozen flow at the throat. The results also indicated that the electron density increased as the probe was swept towards the centerline of the arc-jet exhaust and decreased as it was moved away from the nozzle exit plane.

A local potential of several volts appeared in the arc-jet exhaust and a dc shift of the zero point of the input voltage and current occured as the probe was traversed through the jet. This prevented the measurement of electron density profiles using the present equipment. A ground probe will be added to the system and further electron density measurements will be made.

8 Conclusions

8.1 Thrust

The results of the 30 kw water-cooled hydrogen arc-jet thrust work indicate:

1. The double pendulum thrust stand gives reliable thrust measurements.
2. A slight zero shift of the system occurs during the tests.
3. The spread of data increases with increasing power.
4. The spread of data is attributable to the heating of the thrust stand components and/or the force transducer.

Preliminary thrust measurements on the 30 kw radiation-cooled arc-jets indicated a significant zero shift problem. It is concluded that the force transducer was temperature sensitive and should be thermally isolated.

8.2 Stagnation enthalpy and mass flux

The test results showed:

1. That local stagnation enthalpies can be measured in the exhaust of a 30 kw hydrogen arc-jet using a water-cooled probe without physical deterioration or damage under local stagnation enthalpy levels up to approximately 90,000 B/lb. (This was the centerline enthalpy for the 61,000 B/lb bluk average stagnation enthalpy tests.)
2. The measured stagnation enthalpy values reproduce and compare favorably with the values predicted from an energy balance.
3. The discrepancy between the measured propellant mass flow and the integrated mass flux indicates that the present probe design is inadequate for local mass flux measurements. The discrepancy may be due to the characteristics of the local flow field at the probe inlet.
4. Separate stagnation enthalpy and mass flux probes are desirable. This is due to the incompatibility of the sharp leading edge requirements of the mass flux probe and the larger leading edges necessitated by the cooling requirements of the enthalpy probe.

8.3 Photometric velocity

The results of the photometric velocity experiments indicate:

1. The present velocity measurements are sensitive to the frequency of the signal.
2. The recording of the photomultiplier output signals on tape introduced an uncertainty in the results.
3. A need exists for determining the validity of the calculated velocities from the velocity meter data.
4. A high frequency correlator should alleviate the frequency sensitivity and taping

problems and determine the validity of the velocities calculated from the velocity meter data.

8.4 Electron beam

The present apparatus does not possess sufficient sensitivity and the necessary reproducibility to obtain meaningful density profiles in a hydrogen arc-jet exhausting into a vacuum of 2 torr.

8.5 Langmuir probe

The Langmuir probe experiments showed that meaningful electron densities can be measured in the nozzle exit exhaust plane of 30 kw hydrogen arc-jets.

9 Appendices

Tables 9.1 thru 9.4 summarize all of the hydrogen arc-jet tests performed in the laboratory for the diagnostic experiments. The arc-jet was operated at more than one condition in several tests. Numerous points were taken within the ranges given in Table 2.2 page 7.

Table 9.1 Arc-jet operating conditions for thrust stand tests

Test no.	Hydrogen flow rate (lb/sec x 10^4)	Power input (kw)	Exit plane stagnation enthalpy (B/lb)	Thermal efficiency (%)	Chamber pressure (torr)
63	3.52	27.2	51,800	69.0	219
64	3.52	27.0	51,400	69.5	217
65	3.52	17–27	29,600–51,000	61–69	191–214
66	3.47	17–27	30,500–51,800	61–69	190–214
67	3.06–4.68	26–30	41,800–57,100	68.5	197–267
68	3.08–4.72	26–30	40,300–58,500	66–70	203–273
69	3.33–4.77	29–33	44,200–60,400	67–71	217–279
70	3.11–4.77	28–33	42,900–61,600	65–70	209–279
71	3.90	30.5	52,400	69.0	242
72	3.11–4.72	23–26	34,600–50,400	64–69	195–265
73	3.08–4.72	23–27	34,600–51,000	64–68	195–266
74	3.55	17–29	30,200–53,100	61–69	196–221
75	3.52	17–29	28,700–53,800	59–69	192–219
76	2.93–4.76	25–30	39,000–59,500	64–70	194–275
77	2.91–4.71	26–30	39,000–57,100	64–70	191–268
78	2.91–4.71	28–32	41,600–51,100	63–70	197–272
79	3.00–4.53	28–32	45,200–64,400	66–70	203–272
81	3.00–4.85	23–27	33,400–51,100	63–67	186–268
82	2.97–4.85	23–27	33,400–51,600	63–67	186–265
83	3.58	24–27	43,500–49,700	64–69	211–265

Table 9.1 Arc-jet operating conditions for thrust stand tests (continued)

Test no.	Hydrogen flow rate (lb/sec x 10^4)	Power input (kw)	Exit plane stagnation enthalpy (B/lb)	Thermal efficiency (%)	Chamber pressure (torr)
84	3.57	17–27	28,400–49,600	58–68	192–214
85	2.95–4.79	26–30	37,800–57,800	63–67	197–270
86	2.95–4.79	25–30	38,400–57,500	64–68	189–270
89	2.97–4.85	23–27	32,300–49,500	61–66	188–268
96	4.02	18–27	34,700–50,100	77	197–215
97	4.51	20–30	34,100–49,100	77.5	215–268
98	4.95–5.43	19–29	30,600–40,800	78.5	226–271
99	5.40	20–31	29,200–43,500	79.0	243–265
100	3.97–5.38	19–30	29,600–52,900	76–79	190–257

Table 9.2 Arc-jet operating conditions for stagnation enthalpy probe tests

Test no.	Hydrogen flow rate (lb/sec x 10^4)	Power input (kw)	Exit plane stagnation enthalpy (B/lb)	Thermal efficiency (%)	Chamber pressure (torr)	Vacuum pressure (torr)
106	4.46	22.0	38,100	78.3	220	1.10
107	4.44	22.0	38,300	78.2	224	1.10
108	4.39	25.0	44,500	80.0	229	1.00
109	4.44	23.0	40,300	79.0	218	1.00
110	4.42	23.3	41,200	79.5	217	1.00
111	4.40	21.9	38,500	78.5	214	1.00
112	4.38	22.0	38,500	77.9	211	1.00
113	4.38	22.0	38,800	78.8	212	1.00
114	4.37	22.0	39,200	79.1	220	1.10
115	3.47	22.0	47,000	75.4	200	0.52
116	3.47	28.0	59,200	75.6	200	0.55
117	4.44	22.4	39,600	79.6	221	1.00
117	3.62	22.3	45,500	75.8	186	0.51
118	3.56	29.0	60,000	76.0	200	0.55
119	4.41	22.0	39,100	79.4	224	1.00
119	3.54	21.8	45,100	75.2	188	0.51

Table 9.3 Arc-jet operating conditions for velocity meter tests

Test no.	Hydrogen flow rate ($lb/sec \times 10^4$)	Power input (kw)	Exit plane stagnation enthalpy (B/lb)	Thermal efficiency (%)	Chamber pressure (torr)	Vacuum pressure (torr)
1	4.78	22.8	38,300	81.4	251	1.40
1	3.54	26.9	53,700	72.6	260	1.40
1	3.54	26.7	57,200	77.3	215	0.70
2	3.57	24.8	52,500	77.5	210	0.92
3	3.57	24.9	52,700	77.0	211	0.40
3	3.57	23.4	49,300	76.9	207	0.38
4	3.52	27.0	57,700	77.0	216	0.46
4	3.57	27.0	57,300	77.5	225	0.52
5	3.48	27.0	58,500	77.6	215	0.44
6	3.57	27.7	59,100	78.3	216	0.46
6	3.57	21.5	46,100	78.1	202	0.46
7	3.51	26.0	55,900	77.6	214	0.44
8	3.55	26.2	56,100	77.9	215	0.42
9	3.53	26.3	56,700	78.3	215	0.43
9	3.54	20.5	43,700	77.0	202	0.42
10	3.48	26.0	56,600	77.8	215	0.42
10	3.48	20.6	33,700	77.0	201	0.42
11	3.43	20.3	45,700	77.7	199	0.43
12	3.53	20.6	44,500	77.8	200	0.40
13	3.47	20.5			199	0.38
14	3.51	20.4			201	0.38
14	3.51	25.5			216	0.38
15	3.53	20.6			200	0.40
16	3.53	20.4	43,900	77.5	202	0.42
17	3.50	20.4	44,300	77.4	201	0.39
18	3.54	20.5	48,400	80.0	201	0.40
19	3.56	20.3	48,500	80.5	201	0.45
20	3.56	20.4	48,800	81.0	201	0.44
21	3.57	21.3	44,800	76.2	188	0.48
22	3.55	22.0	47,000	77.5	191	0.45
23	3.55	21.6	46,900	78.7	191	0.46
23	3.55	26.5	56,200	77.5	203	0.44
24	3.55	27.0	57,100	77.5	206	0.43
25	3.56	20.6	56,400	77.5	191	0.46
25	3.56	27.0	57,400	77.7	206	0.43
26	3.56	20.4	43,800	78.0	190	0.44
26	3.56	26.5	56,300	77.7	206	0.43
27	3.56	21.3	45,600	78.0	180	0.55

Table 9.3 Arc-jet operating conditions for velocity meter tests (continued)

Test no.	Hydrogen flow rate (lb/sec x 10^4)	Power input (kw)	Exit plane stagnation enthalpy (B/lb)	Thermal efficiency (%)	Chamber pressure (torr)	Vacuum pressure (torr)
28	3.56	22.0	45,100	76.7	186	0.50
29	3.55	22.0	45,700	75.8	186	0.45
30	3.57	29.4	60,000	75.0	200	0.56
31	3.57	29.5	61,300	76.4	200	0.55
32	3.55	29.4	61,700	76.8	200	0.53
43	3.57	29.5	60,200	75.3	200	0.49
44	3.57	29.5	60,700	75.7	200	0.47
45	3.57	23.3	47,900	75.4	186	0.47
45	3.57	29.2	60,200	75.9	200	0.47
46	3.57	22.8	47,200	75.6	187	0.47
46	3.57	24.8	51,300	75.8	191	0.47
46	3.57	27.9	57,500	75.8	197	0.47
46	3.57	29.5	60,800	75.7	200	0.47

Table 9.4 Arc-jet operating conditions for Langmuir probe tests

Test no.	Hydrogen flow rate (lb/sec x 10^{-4})	Power input (kw)	Exit plane stagnation enthalpy (B/lb)	Thermal efficiency (%)	Chamber pressure (torr)	Vacuum pressure (torr)
33	3.52	21.0	45,000	77.1	182	0.56
34	3.48	20.8	44,900	76.9	182	0.55
35	3.55	22.5	47,600	76.7	187	0.55
36	3.49	22.6	48,600	76.6	187	0.53
37	3.53	22.7	48,100	76.7	187	0.58
38	3.72	23.3	47,100	77.0	186	0.74
39	3.69	23.3	47,200	76.7	186	0.72
40	3.69	23.2	46,800	76.3	186	0.72
41	3.67	23.0	47,000	76.5	186	0.72
42	3.67	23.0	46,900	76.3	186	0.72
47	3.50	22.5	47,900	76.1	188	0.47
48	3.48	22.8	48,600	76.2	188	0.45
49	3.48	22.4	47,800	75.8	187	0.43
50	3.48	22.5	48,100	76.0	187	0.42
51	3.45	22.7	48,600	75.6	187	0.43
52	3.60	23.6	48,200	76.0	191	0.47
53	3.60	22.8	47,200	76.2	190	0.47

Table 9.4 Arc-jet operating conditions for Langmuir probe tests (continued)

Test no.	Hydrogen flow rate (lb/sec x 10^4)	Power input (kw)	Exit plane stagnation enthalpy (B/lb)	Thermal efficiency (%)	Chamber pressure (torr)	Vacuum pressure (torr)
54	3.60	22.3	46,700	77.2	191	0.45
55	3.60	22.0	46,800	77.8	192	0.45
56	3.60	28.1	59,700	78.5	204	0.45
57	3.60	29.0	60,400	77.1	205	0.47
58	3.60	29.3	60,900	77.0	205	0.45
59	3.60	29.1	60,600	77.1	205	0.45
60	3.60	29.3	60,900	77.3	205	0.45
61	3.60	29.0	60,500	77.2	204	0.45
62	3.60	29.0	60,400	77.1	204	0.45

Table 9.5 Sample data for enthalpy probe tests

Table 9.5 is a tabulation of the measurements obtained with the total enthalpy probe for a typical exit plane profile.

The measurements taken at each radial position are the hydrogen pressure and temperature before the sonic flow nozzle, three cooling water flow rates and the corresponding three cooling water temperature differentials. The total enthalpy is then calculated from these measurements.

The data in Table 9.5 refer to Test 118 and the following conditions:

Exit flow nozzle diameter	0.171 inches
Hydrogen flow rate	3.56×10^{-4} lb/sec
Voltage	141 volts
Current	205 amps
Power input	29 kw
Efficiency	76%
Exit plane stagnation enthalpy	60,000 B/lb

R (inches)	P_∞ (psia)	T_∞ (°R)	$\dot{m}_{H_2}$ (lb/sec)	$\dot{w}_1$ (lb/sec)	ΔT_1 (°R)	$\dot{w}_2$ (lb/sec)	ΔT_2 (°R)	$\dot{w}_3$ (lb/sec)	ΔT_3 (°R)	h_s (B/lb)
℄	0.230	750.0	2.51×10^{-5}	0.0369	14	0.0239	17	0.0470	27	87,300
−0.1	0.230	836.2	2.41×10^{-5}	0.0253	14	0.0239	16	0.0433	27	79,000
−0.2	0.023	861.7	2.35×10^{-5}	0.0253	12	0.0239	14	0.0361	25	65,600
−0.3	0.221	861.7	2.26×10^{-5}	0.0253	7	0.0247	12	0.0272	23	48,600
−0.4	0.191	861.7	1.96×10^{-5}	0.0261	0	0.0247	6	0.0198	19	26,700
−0.5	0.135	785.6	1.42×10^{-5}	0.0466	0	0.0555	6	0.0198	14	53,000

R = radial position above arc-jet centerline

P_∞ = pressure before sonic flow nozzle

T_∞ = temperature before sonic flow nozzle

$\dot{m}_{H_2}$ = hydrogen flow rate through probe obtained from $P_\infty/\sqrt{T_\infty}$ calibration curve of flow nozzle

$\dot{w}$ = cooling water flow rate

ΔT = temperature rise of cooling water

$$h_s = \frac{(\dot{w}_1 \Delta T_1 + \dot{w}_2 \Delta T_2 + \dot{w}_3 \Delta T_3)}{\dot{m}} = \text{stagnation enthalpy}$$

10 Distribution list

Name and Address	No. of Copies
1. NASA Lewis Research Center Mail Stop 21–5 21000 Brookpark Road Cleveland, Ohio, 44135 Attn: H. Hunczak	8
2. NASA Lewis Research Center Spacecraft Technology Procurement Section 21000 Brookpark Road Cleveland, Ohio 44135 Attn: J. DeFord	1
3. NASA Lewis Research Center Library 21000 Brookpark Road Cleveland, Ohio 44135	2
4. NASA Lewis Research Center 21000 Brookpark Road Cleveland, Ohio 44135 Attn: J. Jack	1
5. NASA Ames Research Center Moffett Field, California Attn: Dr. G. Goodwin	1
6. NASA Ames Research Center Library Moffett Field, California 94035	1
7. NASA Goddard Space Flight Center Greenbelt, Maryland 20771 Attn: W. Ioley, Code 623, Bldg. 6	1
8. NASA Marshall Space Flight Center R–RP–DIR Bldg. 4481 Huntsville, Alabama 35812 Attn: G. Heller	1
9. NASA Marshall Space Flight Center R–RP–T Bldg. 4488 Huntsville, Alabama 35812 Attn: K. Schocken	1
10. NASA Marshall Space Flight Center R–RP–DIR Huntsville, Alabama 35812 Attn: Dr. E. Stuhlinger	1

Name and Address	No. of Copies
11. NASA Headquarters FOB–10B 600 Independence Ave., N.W. Washington, D.C. 20546 Attn: RNT/J. Lazar	2
12. Aerospace Research Laboratories Wright Patterson AFB, Ohio 45433 Attn: Mr. Soehnger	1
13. Commander Aeronautical Systems Division Wright-Patterson AFB, Ohio 45433 Attn: AFAPL (APIE)	1
14. Oak Ridge National Laboratories Post Office Box Y Oak Ridge, Tennessee Attn: Dr. E. Shipley	1
15. Headquarters, United States Air Force Office of Scientific Research Washington, D.C. 20525 Attn: Dr. M. Slawsky	1
16. United States Army Research Office (Durham) Box CM Duke Station Durham, North Carolina Attn: Dr. P. Kosting	1
17. Aerospace Corporation P.O. Box 95085 Los Angeles 45, California Library Technical Documents Group	1
18. AVCO Corporation Research and Advanced Development Division 201 Lowell Street Wilmington, Massachusetts Attn: Dr. R. John	1
19. AVCO Corporation 201 Lowell Street Wilmington, Massachusetts Attn: Dr. S. Bennett	1
20. Electro-Optical Systems, Inc. 125 N. Vinodo Avenue Pasadena, California Attn: Dr. R. Buhler	1
21. General Electric Company Elect. Space Prop. Projects Evandale, Ohio Attn: Dr. M. L. Boamberg	1
22. Jet Propulsion Laboratory Pasadena, California 91103 Attn: G. Robillard	1
23. The Marquardt Corporation 16555 Saticoy Street Van Nuys, California Attn: Mr. Russell Page	1
24. NASA – Goddard Space Flight Center Library Greenbelt, Maryland 20771	1
25. Gianinni Scientific Corporation 3839 South Main Street Santa Ana, California Attn: Mr. Adriano Ducati	1

Name and Address	No. of Copies
26. Thrust Systems Co. 1641 Monrovia Costa Nova, California Attn: W. Stoner	1
27. Department of Mechanical Engineering University of Minnesota Minneapolis, Minnesota Attn: Dr. E. Eckert	1
28. NASA Scientific and Technical Information Facility Box 5700 Bethesda 14, Maryland Attn: NASA Representative RQT–2448	1
29. NASA Office of Scientific and Technical Information AFSS–A Washington D. C. 20546	1
30. NASA Marshall Space Flight Center Library Huntsville, Alabama 35812	1
31. NASA Marshall Space Flight Center Building 4488 Huntsville, Alabama Attn: Mr. Dan Gates (MS–T)	1
32. Aeronautical Systems Division Wright Patterson Air Force Base, Ohio Attn: ASRMPE F. L. Hommedien	1
33. NASA Lewis Research Center 21000 Brookpark Road Cleveland, Ohio 44135 Attn: Technology Utilization Office	1
34. NASA – Lewis Research Center Spacecraft Technology Division (MS–21–5) 21000 Brookpark Road Cleveland, Ohio 44135 Attn: J. H. Childs	2
35. AFWL Kirtland Air Force Base, New Mexico Attn: WLPC/Capt. C. F. Ellis	1
36. NASA Lewis Research Center 21000 Brookpark Road Cleveland, Ohio 44135 Reports Control Office	1
37. Westinghouse Astronuclear Laboratories Pittsburg 34, Pennsylvania Attn: H. W. Szymanowski, Manager Electrical Propulsion Laboratory	1
38. Aerojet General San Ramon, California Attn: Dr. J. S. Luce	1
39. AVCO-Everett Research Lab. Everett, Massachusetts Attn: R. M. Patrick	1
40. Philco Corporation Newport Beach, California Attn: R. Spongberg ATC	1